Kinetic Properties of the Cardiac L-Type Ca^{2+} Channel and Its Role in Myocyte Electrophysiology: A Theoretical Investigation

Gregory M. Faber,* Jonathan Silva,[†] Leonid Livshitz,[†] and Yoram Rudy[†]

*Department of Biomedical Engineering, Case Western Reserve University, Cleveland, Ohio; and [†]Cardiac Bioelectricity and Arrhythmia Center and Department of Biomedical Engineering, Washington University, St. Louis, Missouri

ABSTRACT   The L-type Ca^{2+} channel (Ca$_V$1.2) plays an important role in action potential (AP) generation, morphology, and duration (APD) and is the primary source of triggering Ca^{2+} for the initiation of Ca^{2+}-induced Ca^{2+}-release in cardiac myocytes. In this article we present: 1), a detailed kinetic model of Ca$_V$1.2, which is incorporated into a model of the ventricular mycoyte where it interacts with a kinetic model of the ryanodine receptor in a restricted subcellular space; 2), evaluation of the contribution of voltage-dependent inactivation (VDI) and Ca^{2+}-dependent inactivation (CDI) to total inactivation of Ca$_V$1.2; and 3), description of dynamic Ca$_V$1.2 and ryanodine receptor channel-state occupancy during the AP. Results are: 1), the Ca$_V$1.2 model reproduces experimental single-channel and macroscopic-current data; 2), the model reproduces rate dependence of APD, [Na$^+$]$_i$, and the Ca^{2+}-transient (CaT), and restitution of APD and CaT during premature stimuli; 3), CDI of Ca$_V$1.2 is sensitive to Ca^{2+} that enters the subspace through the channel and from SR release. The relative contributions of these Ca^{2+} sources to total CDI during the AP vary with time after depolarization, switching from early SR dominance to late Ca$_V$1.2 dominance. 4), The relative contribution of CDI to total inactivation of Ca$_V$1.2 is greater at negative potentials, when VDI is weak; and 5), loss of VDI due to the Ca$_V$1.2 mutation G406R (linked to the Timothy syndrome) results in APD prolongation and increased CaT.

INTRODUCTION

Most cellular action potential (AP) models compute the membrane potential starting from macroscopic transmembrane ionic currents through large ensembles of ion channels. The ionic currents are computed using the Hodgkin-Huxley (H-H) scheme (1), which represents voltage and time-dependent conductance changes in terms of ''gating variables'' (e.g., activation, inactivation) that are independent of each other. Current understanding of ion-channel gating clearly indicates strong coupling between kinetic gating transitions that cannot be reproduced within the H-H paradigm (2). Also, the H-H formalism does not represent kinetic states of the ion channel (such as open, closed, inactivated) and is therefore not suitable for simulating molecular interactions, ion-channel mutations that alter specific kinetic transitions, or effects of drugs that bind to the channel in a specific conformational state. To overcome these limitations we have developed and introduced into a model of the whole-cell, single-channel based Markov models of cardiac I$_{Na}$ (3,4), I$_{Kr}$ (5,6), and I$_{Ks}$ (6), channels that are major determinants of the ventricular AP. Markov models represent discrete ion-channel states and their interactions; this property allowed us to examine kinetic state transitions of these channels during the AP (2), simulate the cellular arrhythmogenic manifestations of ion-channel mutations (2–5), and study the role of molecular subunit interactions in channel function (2,6). Recently, we used Markov models to study the cellular electrophysiological

effects of state-specific drug binding (to open or inactivated state) in wild-type and mutant cardiac Na$^+$ channels (7). Given the important role of Ca$_v$1.2, the L-type Ca^{2+} channel, in AP generation, rate-dependence (8,9), and conduction (10,11), and its participation in cellular calcium cycling and excitation-contraction (EC) coupling (12), it is important to develop a detailed kinetic model of this channel. Such model could be used to study various aspects of channel gating in the complex interactive cell environment, to predict the effects on the whole-cell AP of state-specific drug binding to the channel, and to simulate the cellular electrophysiological consequences of Ca$_v$1.2 mutations, such as a recently described missense mutation G406R that causes Timothy syndrome and is characterized by QT interval prolongation on the electrocardiogram and arrhythmia development, as well as an array of other organ dysfunction (13,14).

Ca$_v$1.2 gating is both voltage and Ca^{2+} dependent; the time course and magnitude of [Ca^{2+}] near the channel is a major determinant of its inactivation kinetics. In ventricular myocytes, Ca$_v$1.2 interacts with ryanodine receptors (RyR) to trigger Ca^{2+} release from the sarcoplasmic reticulum (SR) through the calcium-induced-calcium-release (CICR) process. The interaction occurs in a restricted subcellular space in triad formations (15,16). Modeling the Ca$_v$1.2 channel kinetics requires representation of the dynamic Ca^{2+} changes in a restricted subspace for calcium. We introduce a subcellular restricted space where Ca$_v$1.2 and RyR interact to generate a Ca^{2+}-transient. Because our interest is in the L-type Ca^{2+} current, its properties, and its role in the cellular AP and arrhythmia, we adopt a global cellular approach in the simulations; that is, the model subcellular space represents a subsarcolemmal space, along the length of the t-tubules,

into which both L-type Ca^{2+} channels and RyR open. Clearly, this approach cannot be used to simulate local microscopic (molecular) processes of EC-coupling such as Ca^{2+} spark formation, as done by others (17,18). However, as shown in the Results section, the model recreates the relevant global properties of calcium cycling that influence the L-type Ca^{2+} current, I$_{Ca(L)}$. This global approach results in major reduction of computing time, making the simulations of steady-state pacing protocols that are necessary for studying cell electrophysiology possible and practical.

Using this model, the following phenomena are studied: 1), kinetic state transitions of Ca$_v$1.2 and RyR during the AP at slow and fast rates; 2), the relative contributions of Ca^{2+}-dependent and voltage-dependent inactivation to total inactivation of I$_{Ca(L)}$; 3), sensitivity of Ca^{2+}-dependent inactivation to Ca^{2+} entry through the channel and from SR release; 4), rate dependence of AP duration (APD adaptation) and APD restitution; 5), rate dependence of [Na$^+$]$_i$ and of the Ca^{2+}-transient; restitution of the Ca^{2+}-transient during premature stimuli; 6), I$_{Ca(L)}$ and AP modification by the Ca$_v$1.2 missense mutation G406R that has been associated with the Timothy syndrome and its arrhythmic manifestations.

METHODS

A complete list of abbreviations, parameter definitions, model equations, and initial conditions can be found in Table 1 and the Appendix.

L-type Ca^{2+} channel Markov model

A Markov representation of the L-type Ca^{2+} channel (Fig. 1) was developed and incorporated into a ventricular cell model. L-type Ca^{2+} channels are known to inactivate due to an increase in membrane potential or an increase in intracellular Ca^{2+}. The former, known as voltage-dependent inactivation (VDI), is accompanied by a gating current whereas the latter, known as Ca^{2+}-dependent inactivation (CDI), is not. This discovery by Hadley and Lederer (19) suggests that the mechanisms by which these inactivation processes occur are separate, implying that channels that have inactivated due to voltage can still be inactivated by Ca^{2+} and vice versa. This is further supported by experiments where VDI or CDI are altered or eliminated by point mutations to the Ca$_V$1.2 gene. This is perhaps best illustrated by the Ca$_V$1.2 mutation G406R, which is the underlying cause of the Timothy syndrome, which almost completely eliminates VDI while leaving CDI unaffected (13,14). VDI of Ca$_V$1.2 is also affected by mutations to the pore-encoding portion of the channel (20) or mutations within the I-II linker (13,21). CDI, which involves Ca^{2+} binding to calmodulin (CaM) that is constitutively tethered to a region of the Ca$_V$1.2 C-terminus known as the IQ motif, is eliminated by mutations to either the IQ motif (22–24) or to CaM (25). There has been recent evidence that VDI may also be dependent on the IQ-CaM complex (26), giving rise to the possibility that VDI and CDI are not entirely independent. We model the channel with two distinct kinetic modes (27,28): a voltage-gating mode (ModeV) with a single conducting state, and a mode where the channel is inactivated via a Ca^{2+}-dependent process (ModeCa). We selected the minimum number of channel states necessary to reflect structural properties of the channel (four voltage sensitive transitions before channel opening reflecting movement of four voltage sensors, one for each of the four homologous domains making up the α_1 subunit of Ca$_V$1.2) and to describe the complex channel behavior (fast and slow voltage-dependent inactivation states, I$_{Vf}$ and I$_{Vs}$, (29)). The two-tier structure (upper tier, ModeV; lower tier, ModeCa) implies that the

channel can be inactivated by Ca^{2+} at any time, independent of the channel being closed, open, or inactivated by voltage. In addition, this means that channels can be simultaneously inactivated via both voltage-dependent and Ca^{2+}-dependent mechanisms. Despite the relatively large number of channel states, the total number of transition rates that must be computed each time step is small (rates computed for state transitions within ModeV are the same for ModeCa and transition rates between ModeV and ModeCa are the same from any state).

Experimental protocols to study L-type Ca^{2+} channels often utilize charge carriers other than Ca^{2+} to separate voltage-dependent inactivation from Ca^{2+}-dependent inactivation. To reproduce these experimental protocols with the model, we eliminate Ca^{2+}-dependent inactivation by setting the transition rates from ModeV to ModeCa to zero. Simulations where this is done are noted in the text and in the figure caption.

The L-type Ca^{2+} channel Markov model was validated utilizing a wide range of experimental data. Our guide was to select experimental data that were recorded in guinea pig ventricular myocytes at 37°C. In addition, we preferentially selected experimental data that were recorded in the absence of β-agonists as these have a significant effect on current magnitude, voltage-dependent properties, and Ca^{2+}-dependent properties of the channel.

The L-type Markov model (Fig. 1) includes four closed states (C$_0$, C$_1$, C$_2$, and C$_3$), a single open state (O), two states representing channels that have undergone fast or slow voltage-dependent inactivation (I$_{Vf}$ and I$_{Vs}$), five states representing channels that have undergone Ca^{2+}-dependent inactivation (C$_{0Ca}$, C$_{1Ca}$, C$_{2Ca}$, C$_{3Ca}$, and I$_{Ca}$), and two states that represent inactivation via both voltage and Ca^{2+}-dependent mechanisms (I$_{VfCa}$ and I$_{VsCa}$). The transition rates in each loop of the model (e.g., C$_3$-O-I$_{Vs}$) obey microscopic reversibility.

Cell model

The theoretical LRd model of a mammalian ventricular AP (30–32) (Fig. 2 A) provides the basis for the simulations of cellular behavior in this study. The model is based mostly on guinea pig ventricular myocyte experimental data; it includes membrane ionic channel currents, pumps, and exchangers. The model also accounts for processes that regulate intracellular concentration changes of Na$^+$, K$^+$, and Ca^{2+}. Intracellular Ca^{2+} cycling processes represented in the model include Ca^{2+} uptake and release by the SR and its buffering. Buffers include calmodulin and troponin (in the myoplasm), sarcolemmal and SR Ca^{2+} binding sites (in the subspace), and calsequestrin (in the SR).

Subspace compartment

Electron microscopic views of myocytes reveal invaginations in the cell membrane, known as transverse or t-tubules, that increase the total surface area of the myocyte and provide a pathway by which extracellular Ca^{2+} can be readily available for entry upon cell depolarization. The junctional sarcoplasmic reticular membrane makes close contact with sarcolemmal membrane all along the t-tubules, the distance between the two membranes being very small (15–20 nm). The confined volume between the two membranes is commonly referred to as the restricted space or the subsarcolemmal space. It is known that Ca^{2+} entry via L-type Ca^{2+} channels is the signal for the opening of RyRs and Ca^{2+} release from the SR. Immunogold-labeling techniques (33,34) have shown that L-type Ca^{2+} channels cluster in t-tubules and the areas of the plasma membrane that overlie the SR membrane, supporting their important role in the CICR process. Ca^{2+} entry into the restricted space via L-type Ca^{2+} channels (followed closely by Ca^{2+} release from the SR) generates Ca^{2+} concentrations near the inner membrane surface that are much greater than those observed in the bulk myoplasm. The magnitude of these concentrations and the rate at which the concentrations return to basal levels is dependent upon several factors including: 1), subspace volume; 2), Ca^{2+} diffusion rates from the subspace to the bulk myoplasmic volume; 3), the presence of buffers within the subspace; 4), the rate of Ca^{2+} entry into the subspace (i.e., via L-type and RyR channels); and 5), the rate of Ca^{2+}

TABLE 1 Definitions and abbreviations

AP	Action potential
APD	Action potential duration measured at 90% repolarization
BCL	Basic cycle length
$Ca_V1.2$	Cardiac L-type Ca^{2+} channel
RyR	Ryanodine receptor SR Ca^{2+} release channel
CaT	Calcium transient
CICR	Calcium induced calcium release
VDI	Voltage-dependent inactivation
CDI	Calcium-dependent inactivation
ModeV	L-type Ca^{2+} channel states in VDI gating mode
ModeCa	L-type Ca^{2+} channel states in CDI gating mode
I_{Na}	Fast Na^+ current, $\mu A/\mu F$
m	Activation gate of I_{Na}
h	Fast inactivation gate of I_{Na}
j	Slow inactivation gate of I_{Na}
$I_{Ca(L)}$	Ca^{2+} Current through L-type Ca^{2+} channel, $\mu A/\mu F$
$I_{Ca,Na}$	Na^+ Current through L-type Ca^{2+} channel, $\mu A/\mu F$
$I_{Ca,K}$	K^+ Current through L-type Ca^{2+} channel, $\mu A/\mu F$
I_{Kr}	Rapid delayed rectifier K^+ current, $\mu A/\mu F$
x_r	Activation gate of I_{Kr}
r_{Kr}	Time-independent rectification gate of I_{Kr}
I_{Ks}	Slow delayed rectifier K^+ current, $\mu A/\mu F$
x_{s1}	Fast activation gate of I_{Ks}
x_{s2}	Slow activation gate of I_{Ks}
I_{K1}	Time-independent K^+ current, $\mu A/\mu F$
K_1	Inactivation gate of I_{K1}
I_{Kp}	Plateau K^+ current, $\mu A/\mu F$
$I_{Ca,b}$	Background Ca^{2+} current, $\mu A/\mu F$
$I_{Ca(T)}$	T-Type Ca^{2+} current, $\mu A/\mu F$
$I_{Na,b}$	Background Na^+ current, $\mu A/\mu F$
I_{NaCa}	Na^+-Ca^{2+} exchanger in myoplasm, $\mu A/\mu F$
$I_{NaCa,ss}$	Na^+-Ca^{2+} exchanger in subspace, $\mu A/\mu F$
γI_{NaCa}	Position of energy barrier controlling voltage dependence of I_{NaCa}
I_{NaK}	Sodium-potassium pump, $\mu A/\mu F$
f_{NaK}	Voltage-dependent parameter of I_{NaK}
σ	$[Na^+]_o$ dependent factor of I_{NaK}
$I_{p,Ca}$	Sarcolemmal Ca^{2+} pump, $\mu A/\mu F$
$\overline{G}_x$	Maximum conductance of channel x, $mS/\mu F$
K_m	Half-saturation concentration, mM/L
P_S	Membrane permeability to ion S, cm/s
$P_{S,A}$	Permeability ratio of ion S to ion A
γ_S	Activity coefficient of ion S
$\overline{I}_x$	Maximum current carried through channel x, $\mu A/\mu F$
V_m	Transmembrane potential, mV
z_s	Valence of ion S
C_m	Total cellular membrane capacitance, $1\ \mu F$
A_{Cap}	Capacitive membrane area, cm^2
A_{Geo}	Geometric membrane area, cm^2
R_{CG}	Ratio of $A_{Cap}/A_{Geo} = 2$
V_x	Volume of compartment x, μL
$\Delta[S]_x$	Change in concentration of ion S in compartment x, mM
CASQ2	Calsequestrin, Ca^{2+} buffer in JSR
TRPN	Troponin, Ca^{2+} buffer in myoplasm
CMDN	Calmodulin, Ca^{2+} buffer in myoplasm
BSR	Anionic SR binding sites for Ca^{2+} in the subspace
BSL	Anionic sarcolemmal binding sites for Ca^{2+} in the subspace
SR	Sarcoplasmic reticulum
JSR	Junctional SR
NSR	Network SR
ss	Subspace
myo	Myoplasm
E_x	Reversal potential of current x, mV

(Continued)

TABLE 1 (Continued)

$[S]_o$	Extracellular concentration of ion S, mM
$[S]_i$	Intracellular concentration of ion S, mM
$[S]_{ss}$	Subspace concentration of ion S, mM
$[Ca^{2+}]_{JSR}$	Ca^{2+} concentration in JSR, mM
$[Ca^{2+}]_{JSR,t}$	Total Ca^{2+} concentration in JSR ($[Ca^{2+}]_{JSR}$ + $[csqn]$), mM
$[Ca^{2+}]_{NSR}$	Ca^{2+} concentration in NSR, mM
I_{rel}	Ca^{2+} release from JSR to subspace, mM/ms
$adap$	Function describing RyR channel adaptation
$gradedrel$	$I_{Ca(L)}$ dependent function for determining graded response of I_{rel}
$vgainofrel$	Function describing voltage dependence of gain
I_{up}	Ca^{2+} uptake from myoplasm to SR, mM/ms
I_{leak}	Ca^{2+} leak from NSR to myoplasm, mM/ms
I_{tr}	Ca^{2+} transfer from NSR to JSR, mM/ms
τ_{tr}	Time constant of Ca^{2+} transfer from NSR to JSR, ms
I_{diff}	Ca^{2+} transfer from subspace to myoplasm, mM/ms
τ_{diff}	Time constant of Ca^{2+} transfer from subspace to myoplasm, ms
$F_{I_{Ca(L)}}$	Ca^{2+} flux from $I_{Ca(L)}$
F_{rel}	Ca^{2+} flux from I_{rel}
F	Faraday constant, 96,487 C/mol
R	Gas constant, 8314 J/kmol/K
T	Temperature, 310°K
τ_0	Rate constant of monoexponential decay for the probability density function fit to the open probability data of the L-type Ca^{2+} channel
$I_{Ca,t}$	Total transmembrane Ca^{2+} current $I_{Ca,t} = I_{Ca(L)} + I_{Ca,b} + I_{p,Ca} - 2*I_{NaCa} - 2*I_{NaCass}$
$I_{Na,t}$	Total transmembrane Na^+ current $I_{Na,t} = I_{Na} + I_{Na,b} + 3*I_{NaK} + I_{Ca,Na} + 3*I_{NaCa} + 3*I_{NaCass}$
$I_{K,t}$	Total transmembrane K^+ current $I_{K,t} = I_{Ks} + I_{Kr} + I_{K1} + I_{Ca,K} + I_{Kp} - 2*I_{NaK}$
I_{tot}	Total transmembrane current $I_{tot} = I_{Ca,t} + I_{Na,t} + I_{K,t}$
I_{stim}	Stimulus current, $\mu A/\mu F$

removal (i.e., via forward Na^+/Ca^{2+} exchange). We model the subspace as a single compartment comprising 2% of the total volume of the myocyte into which both L-type Ca^{2+} channels and RyR open (see Appendix for derivation of subspace volume). Immunofluorescence of the Na^+-Ca^{2+} exchange protein (35,36) has shown that these proteins are present with greater density within the t-tubules, hence 20% of the Na^+-Ca^{2+} exchanger is included in the modeled subspace (37). Finally, we include sarcolemmal and SR membrane binding sites that buffer calcium (38).

Ryanodine receptor Markov model

A Markov model of the RyR, modified from that originally presented by Fill et al. (39) is utilized in the simulations (Fig. 2 B). The RyR Markov model is based upon experiments by Zahradníková et al. (40) where individual RyR channels were fused into a planar lipid bilayer. This preparation allows for direct control of Ca^{2+} concentrations to determine rates of channel activation and inactivation (an approach that shows that RyR channels both activate and inactivate due to a rise in subspace calcium ($[Ca^{2+}]_{ss}$). In addition, the four transitions necessary to reach the open state reflect the homotetrameric structure of RyR (41). All of the channel transition rates are increased to adjust for the temperature differences between the experiments (23°C) and model (37°C). An addition to the original Fill (39) model is the inclusion of four additional inactivation states (I_1–I_4) connected to the closed

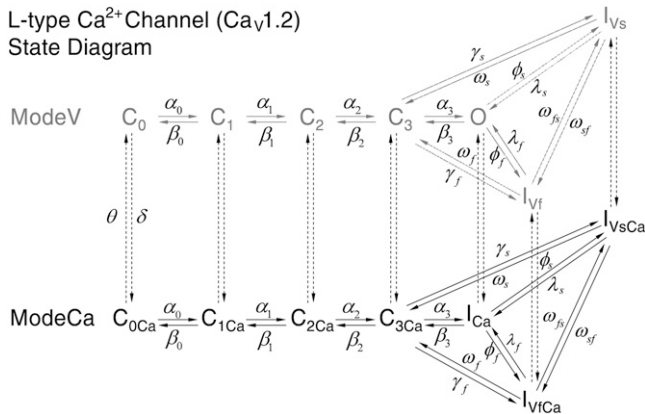## L-type Ca^{2+} Channel (Ca$_V$1.2) State Diagram

FIGURE 1 State diagram of the L-type Ca^{2+} channel Markov model. The upper tier (ModeV, *gray*) represents a voltage-dependent inactivation gating mode (VDI) and the lower tier (ModeCa, *black*) represents a Ca^{2+}-dependent inactivation gating mode (CDI). See Appendix for transition rates.

states (C$_1$–C$_4$). This change allowed RyR channels to deactivate without having to pass through the open state, preventing reopening of the channel during repolarization and during rest. In our simulations, when channels could only recover from inactivation through the open state, Ca^{2+} leaked from the SR for the duration of the AP preventing SR refilling and normal decay of the calcium transient. This behavior could not be observed in the lipid bilayer experiments where RyRs were not stimulated by APs.

It has been suggested that calsequestrin (CASQ2) may also be an important modulator of RyR activity (42,43). CASQ2 is a high-capacity, low-affinity buffer of Ca^{2+} located in the SR. Kawasaki and Kasai (44)
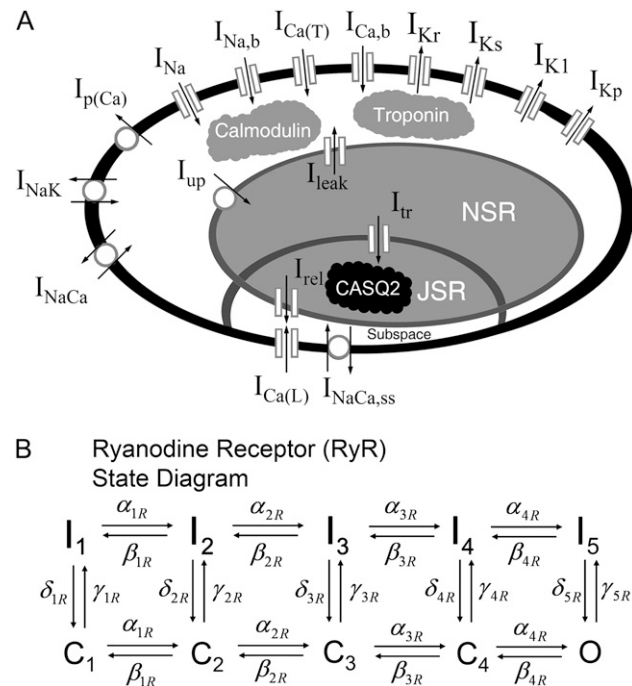

FIGURE 2 (*A*) Schematic for the four compartment model (bulk myoplasm, JSR, NSR, and subspace) of the guinea pig ventricular myocyte. Symbols are defined in Table 1. (*B*) State diagram of the ryanodine receptor, RyR, (modified from Fill et al. (39)). See Appendix for transition rates.
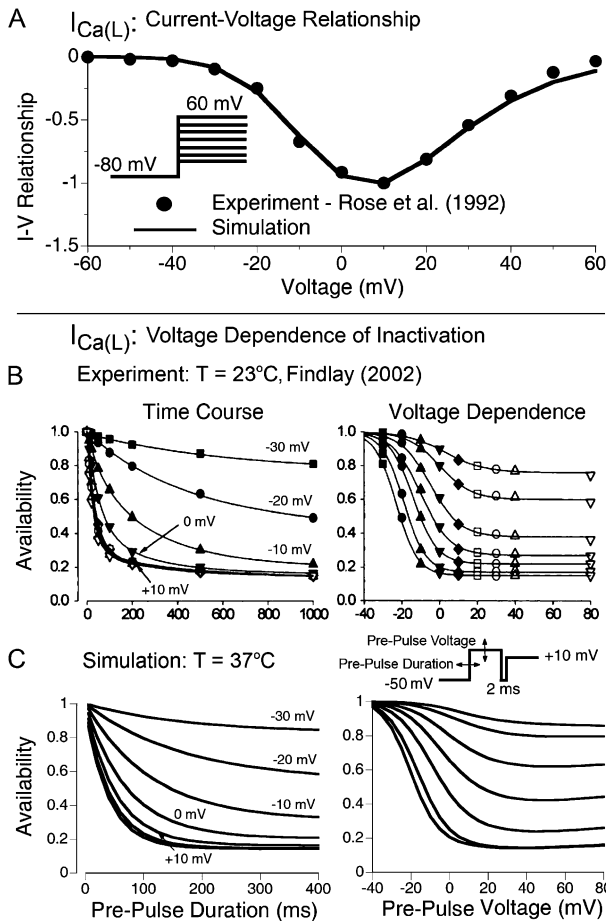
demonstrated that introduction of CASQ2 to the SR increased the RyR open probability and Hidalgo and Donoso (45) showed that interventions that led to conformational change of CASQ2 resulted in opening of RyRs. Studies by Györke et al. (46) showed that low SR Ca^{2+} led to CASQ2 inhibition of RyR opening and that upon elevation of SR Ca^{2+} this inhibition decreased. Communication between CASQ2 and RyR may be mediated by the auxiliary proteins triadin and junctin (47,48). Because RyR channels in the experiments of Zahradníková et al. (40) were studied in isolation, their dependence on CASQ2 was not apparent and hence not incorporated into their Markov model of RyR. We incorporate this dependence into the RyR Markov model presented here.

Simulation protocols

During pacing, a stimulus of -80 μA/μF is applied for a duration of 0.5 ms. The model is paced with a conservative current stimulus carried by K$^+$ (49). A discrete time step of 0.0002 ms is used during computation of the AP (or during voltage clamp simulations) and 0.002 ms during the diastolic interval. APD is measured as the interval between the time of maximum upstroke velocity (dV/dt_{max}) and 90% repolarization (APD).

RESULTS

L-type Ca^{2+} channel: model validation and gating properties

Fig. 3 *A* compares the simulated I$_{Ca(L)}$ current-voltage relationship to the experimentally measured current-voltage relationship (50). L-type Ca^{2+} channels typically begin to activate between -40 and -30 mV and peak current is reached between 0 and $+10$ mV. Fig. 3 *C* shows simulated voltage-dependent inactivation (VDI) properties of I$_{Ca(L)}$ compared to the experimentally measured data reproduced in Fig. 3 *B* (51). To eliminate CDI, Findlay substituted extracellular Ca^{2+} with Mg^{2+}. We eliminate CDI by not permitting transitions from ModeV to ModeCa (setting transition rates to zero). In both model and experiment, channel inactivation increases with increased prepulse voltage and with increased prepulse duration. Because the experiments were conducted at 23°C, the values for the prepulse duration were adjusted to 37°C utilizing a $Q_{10} = 2$ in the simulation. Findlay observed two time constants of inactivation for the L-type Ca^{2+} channel. The model accounts for this observation by including two voltage-dependent inactivation states, one for which transitions into the state are fast (I$_{Vf}$) and one for which transitions are slow (I$_{Vs}$).

The L-type Ca^{2+} channel Markov model recreates single channel properties as shown in Fig. 4. The simulated open time histogram for a voltage step to $+10$ mV (Fig. 4 *A*) can be fit by a monoexponential probability density function with a $\tau_o = 0.8$ ms, in agreement with the experiments of Cavalié et al. (52). The latency to first opening is shown in Fig. 4 *B*, with the simulation showing strong correlation to experimental data by Cavalié et al. (52) who observed >90% channel openings within 6 ms of depolarization. The simulations were conducted without Ca^{2+}-dependent inactivation.

Following SR Ca^{2+} release, Ca^{2+} concentrations within the subspace can reach a value 50 times higher than myoplasmic
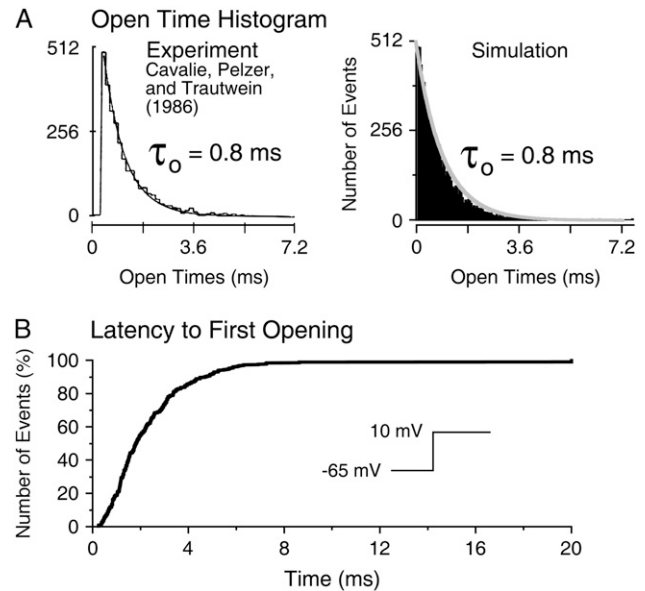
FIGURE 4 Single channel properties of the L-type Ca^{2+} channel. The experimental data (from Cavalié et al. (52), with permission) are from single channel recordings in guinea pig ventricular myocytes at 32°C, and were measured utilizing Ba^{2+} as the charge carrier. To model Ba^{2+} as the charge carrier, all simulations were conducted without transitions to ModeCa. (A) Simulated (left) and experimental (right) (52) open time histograms measured for a voltage step to $+10$ mV from a holding potential of -65 mV (B, inset). The open probability data were fit by a monoexponential probability density function with a time constant of $\tau_0 = 0.8$ for both measured and simulated data. (B) Simulated latency to first opening. Channels are simulated with the same square pulse protocol as panel A.

FIGURE 3 L-type Ca^{2+} channel current-voltage relationship and voltage-dependent inactivation. (A) Simulated $I_{Ca(L)}$ current-voltage relationship (normalized) compared to experimental data recorded in guinea pig ventricular myocytes (from Rose et al. (50), with permission) (●). (B and C) Voltage-dependent inactivation (VDI) of $I_{Ca(L)}$ obtained from a double-pulse protocol (inset). The simulations are conducted in the absence of Ca^{2+}-dependent inactivation (transitions from ModeV to ModeCa are prevented). Panels (B) show experimental time course (left) and voltage dependence (right) of VDI recorded in guinea pig ventricular myocytes at 23°C (Findlay (51), with permission) utilizing Mg^{2+} as the charge carrier. The voltage dependence curves (right panel), from upper to lower, correspond to prepulse durations of 10, 20, 50, 100, 200, 500, and 1000 ms. Panels (C) show the corresponding simulated time course and voltage dependence of VDI. The voltage dependence curves, from upper to lower, correspond to prepulse durations of 4, 8, 20, 40, 80, 200, and 400 ms (the simulations are conducted for body temperature, 37°C).

concentrations. Therefore, the L-type Ca^{2+} channel Markov model must be responsive to large changes in Ca^{2+}. Fig. 5 A shows the sensitivity of $I_{Ca(L)}$ to $[Ca^{2+}]_{ss}$, both simulated and experimentally measured (53). It should be noted that the experimental data are a measure of single channel activity, while the simulated data are a measure of peak $I_{Ca(L)}$. There is a strong correlation between the simulated and experimental data, both exhibiting a $K_D = 3$ μM. In addition, for both experiment and model, even for very high concentrations of subspace Ca^{2+}, the channel does not inactivate

completely (to zero). In the simulation (and experiment), the tested $[Ca^{2+}]_{ss}$ was applied and the model was allowed to reach steady state at that concentration before application of the square pulse. Hence, this study provides the steady-state dependence of $I_{Ca(L)}$ on $[Ca^{2+}]_{ss}$ and gives no indication of the time course of Ca^{2+}-dependent inactivation. This time course was determined by optimizing the morphology of $I_{Ca(L)}$ during the AP clamp protocol shown in Fig. 8, where SR release was kept intact. The time course of $I_{Ca(L)}$ recovery from Ca^{2+}-dependent inactivation is shown in Fig. 5 B. The experimental data (solid circles) (54) were measured in guinea pig ventricular myocytes at 35°C with SR Ca^{2+} release intact. The experimentally measured time constant of recovery is $\tau = 92$ ms, and the model time constant of recovery is $\tau = 101$ ms. When we eliminate CDI in the model, the time constant of recovery shows only a slight decrease ($\tau = 88$ ms). This is in agreement with experimental results that show no significant difference in the rate of $I_{Ca(L)}$ recovery when utilizing either Ca^{2+} or Ba^{2+} as the charge carrier (Ian Findlay, PhD, Université de Tours, France personal communication, 2004).

The relative contribution of CDI to total $I_{Ca(L)}$ inactivation is shown in Fig. 6 for two different times (t_{early} and t_{late}) after application of a voltage step. CDI's contribution to inactivation is computed as the ratio of inactivation with Ca^{2+} as
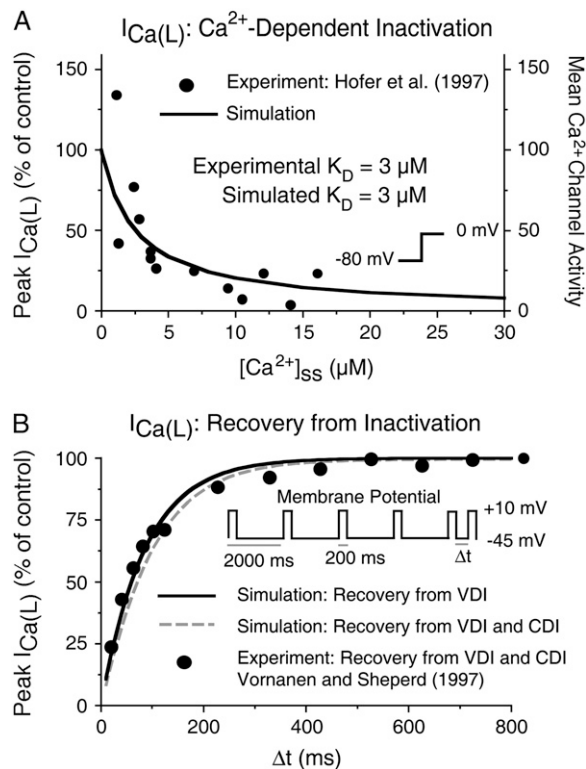
FIGURE 5   (A) Dependence of peak $I_{Ca(L)}$ on intracellular subspace Ca^{2+}. Values are normalized to control conditions of $[Ca^{2+}]_{ss} = 0.02\ \mu M$. For each value of $[Ca^{2+}]_{ss}$, the channel is allowed to reach steady state before application of a square voltage pulse to 0 mV. The experimental data (from Höfer et al. (53), with permission) (●) provide normalized channel activity recorded utilizing a cell attached patch in guinea pig ventricular myocytes at 37°C. (B) $I_{Ca(L)}$ recovery from inactivation. The experimental data (from Vornanen and Shepherd (54), with permission) (●) were recorded in guinea pig ventricular myocytes at 35°C utilizing Ca^{2+} as the charge carrier with a time constant of recovery $\tau = 92$ ms. The solid curve shows simulated $I_{Ca(L)}$ recovery from VDI (no transitions to ModeCa; non-Ca^{2+} charge carrier) with a time constant of recovery $\tau = 88$ ms. The gray dashed curve shows simulated $I_{Ca(L)}$ recovery from both VDI and CDI (Ca^{2+} as the charge carrier) with a time-constant of recovery $\tau = 101$ ms.

the charge carrier relative to the inactivation when Ba^{2+} is the charge carrier. The experimental data (*solid squares*) (55) were recorded at room temperature (23°C) so the time at which the data are sampled is adjusted to 37°C in the simulation (Experiment: $t_{early} = 20$ ms, $t_{late} = 200$ ms; Simulation: $t_{early} = 8$ ms, $t_{late} = 80$ ms). The relative contribution of CDI to total inactivation is both voltage dependent and time dependent. CDI is responsible for a greater percentage of inactivation at negative potentials when VDI is weak and in the period shortly after depolarization. With increased time and voltage, the contribution of CDI to total inactivation decreases and VDI becomes dominant.

The rate of transition between ModeV and ModeCa is dependent on the Ca^{2+} concentration within the subspace ($[Ca^{2+}]_{ss}$). The relative contribution to CDI of Ca^{2+} that enters the subspace via $I_{Ca(L)}$ versus that which enters the subspace via SR release is explored in Fig. 6, C–F. In the

simulation and experiment (8) (Fig. 6, *C* and *D*, respectively), cells are clamped from holding potential to −10 mV for the trace where Ca^{2+} is not the charge carrier (*trace 3*) and from holding potential to 0 mV for the two traces where Ca^{2+} is the charge carrier (*traces 1* and *2*). In the experiment (Fig. 6 *D*, *trace 2*), SR Ca^{2+} release is blocked with the application of ryanodine that we simulate by setting $I_{rel} = 0$ (Fig. 6 *C*, *trace 2*). In summary, trace 1 represents total $I_{Ca(L)}$ inactivation (VDI + CDI from $I_{Ca(L)}$ and I_{rel}), trace 2 represents $I_{Ca(L)}$ inactivation in the absence of SR release (VDI + CDI from $I_{Ca(L)}$ only), and trace 3 represents pure VDI (no CDI). Fig. 6, *E* and *F* show the percent contribution to CDI from SR release ((*trace 2 − trace 1*)/(*trace 3 − trace 1*)) compared to the percent contribution to CDI from Ca^{2+} entering via $I_{Ca(L)}$ ((*trace 3 − trace 2*)/(*trace 3 − trace 1*)). It is clear that Ca^{2+} released from the SR dominates CDI initially, then, as Ca^{2+} decreases due to SR reuptake of Ca^{2+}, the SR dependent contribution declines with participation from Ca^{2+} entry via $I_{Ca(L)}$ dominating. For the simulated time period shown in Fig. 6 *E* RyRs open quickly, inactivate, and then remain almost fully inactivated; thus, there is very little steady-state SR-dependent contribution to CDI, as appears to be the case in the SR-dependent experimental curve of Fig. 6 *F*. Reasons for this observed difference can be attributed to the fact that the experimental data were recorded in human atrial cells at room temperature (23°C). Despite these differences, the behavior of the model follows that of the experiment, especially during the initial phase following depolarization when a sharp decline in current is observed, correlating with the large increase in $[Ca^{2+}]_{ss}$ during the period of SR Ca^{2+} release and dominance of SR-dependent inactivation (Fig. 6 *C*, *trace 1*, and *E*, *SR-dependent curve*). This initial fast decline is followed by a much slower decrease in current (Fig. 6 *C*, *trace 1*), a combination of VDI and CDI from Ca^{2+} entry via $I_{Ca(L)}$. The crossover of the SR-dependent and $I_{Ca(L)}$-dependent CDI curves occurs 36 ms after depolarization in the simulation and 55 ms after depolarization in the experiment.

RyR model in the subspace: graded release, fractional release, and variable gain

Communication between L-type Ca^{2+} channels and RyRs occurs in local diadic spaces and the stochastic opening of a single L-type Ca^{2+} channel can trigger the opening of several local RyRs. The magnitude of Ca^{2+} entry via $I_{Ca(L)}$ determines the number of RyR openings, thus small $I_{Ca(L)}$ results in small SR release compared to large $I_{Ca(L)}$ resulting in large SR release. This phenomenon is known as graded release or graded response and is reproduced by the model as shown in Fig. 7 *A*. Note that in our macroscopic formulation the spatial distribution of RyRs is not represented and the ratio of RyR channels that open in response to a given $I_{Ca(L)}$ is introduced to recreate the macroscopic properties of global release.

The model exhibits a steep nonlinear dependence of fractional SR release as a function of JSR Ca^{2+} content as
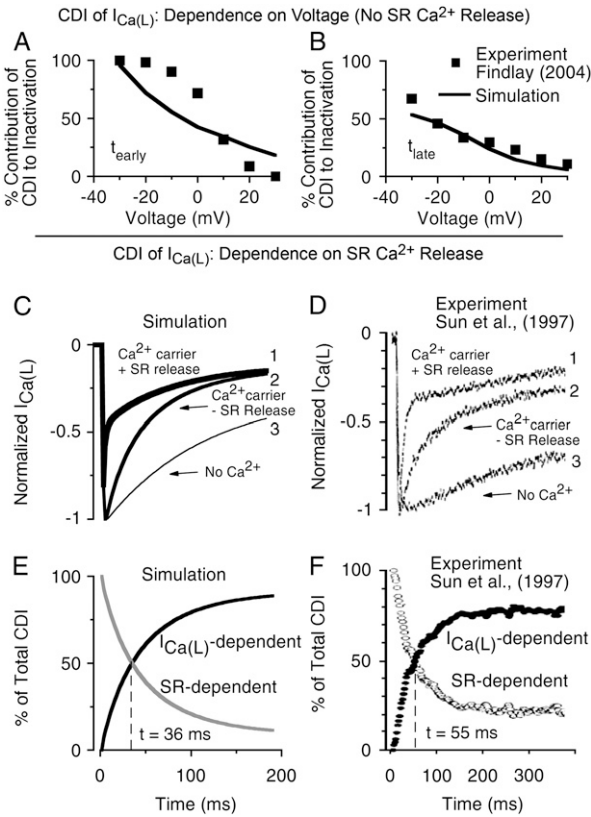
FIGURE 6 (*A* and *B*) Voltage dependence of the contribution of CDI to total inactivation for two different times (early, t_{early}; late, t_{late}) after application of a voltage step to varying potentials from a holding potential of −80 mV. The plotted values are the ratio of current decay recorded with Ca^{2+} as the charge carrier relative to that recorded with Ba^{2+} as the charge carrier. Experiments (from Findlay (55), with permission) (■) were conducted at room temperature (23°C) and simulations (*solid line*) at 37°C; values of t_{early} and t_{late} were adjusted for 37°C in the simulations. (Experiment: $t_{early} = 20$ ms, $t_{late} = 200$ ms; Simulation: $t_{early} = 8$ ms, $t_{late} = 80$ ms). (*C–F*) Relative contributions of Ca^{2+} through the channel and Ca^{2+} released from the SR to total CDI during a voltage step. (*C*) Trace 3 (*thin curve*) shows simulated $I_{Ca(L)}$ in the absence of Ca^{2+}-dependent inactivation, corresponding to current carried by monovalent cations or Ba^{2+}, for a voltage step from −80 to −10 mV. Trace 2 (*medium curve*) shows $I_{Ca(L)}$ with Ca^{2+} as the charge carrier (hence with Ca^{2+}-dependent inactivation) but with no Ca^{2+} release from the SR ($I_{rel} = 0$) for a voltage step from −80 to 0 mV (the 10-mV difference in test potential compared to trace 3 is to reproduce the experimental protocol in panel *D* for comparison). Trace 1 (*thick curve*) shows $I_{Ca(L)}$ for the same square pulse with Ca^{2+} as the charge carrier and SR calcium release intact. (*D*) Experimental recordings of $I_{Ca(L)}$ in human atrial myocytes measured at room temperature. Trace 3 is the current through the channel utilizing monovalent cations as the charge carrier tested with a voltage step from −80 to −10 mV. Trace 2 shows $I_{Ca(L)}$ with Ca^{2+} as the charge carrier but with SR release blocked with ryanodine during a voltage step from −80 to 0 mV. Trace 3 shows $I_{Ca(L)}$ with Ca^{2+} as the charge carrier and SR release intact for the same voltage step. (*E*) Simulated fraction of Ca^{2+}-induced inactivation that results from Ca^{2+} released from the SR (*gray*) or from Ca^{2+} entering via $I_{Ca(L)}$ (*black*). The formula for determining the relative contribution is from Sun et al. (8) where the $I_{Ca(L)}$ dependent fraction = (*trace3* − *trace2*)/(*trace3* − *trace1*) and the SR dependent fraction = (*trace2* − *trace1*)/(*trace3* − *trace1*). (*F*) Experimental fractional contribution of $I_{Ca(L)}$-dependent (*black*) and SR dependent (*white*) Ca^{2+}-induced inactivation of $I_{Ca(L)}$. Experimental curves in panels *D* and *F* are reproduced from Sun et al. (8), with permission.

shown in Fig. 7 *B*, in agreement with experiments (56). In the model, the rate of transition between inactivated and closed states is modulated by Ca^{2+}-bound CASQ2 and when SR content is low, channels are unavailable for opening.

Another property that myocytes exhibit is variable gain. Gain is the ratio between the amount of Ca^{2+} released from the SR and the amount of Ca^{2+} entry into the myocyte that triggers SR release. In myocytes, it has been observed that for the same amount of triggering Ca^{2+}, the magnitude of release can vary as a function of the transmembrane potential. For example, in Fig. 7 *A*, the magnitude of $I_{Ca(L)}$ at $V_m = -10$ mV and at $V_m = +30$ mV is approximately the same, but there is a large difference in the magnitude of the Ca^{2+} transient at these two potentials, with the negative potential exhibiting a larger SR Ca^{2+} release. In Fig. 7 *C* we show the simulated relationship between $[Ca^{2+}]_i$ and $I_{Ca(L)}$ over a range of V_m values (indicated on the *curve*) and compare the model results to experimentally measured data in guinea pig ventricular myocytes (57). From the shape of the curve, it is
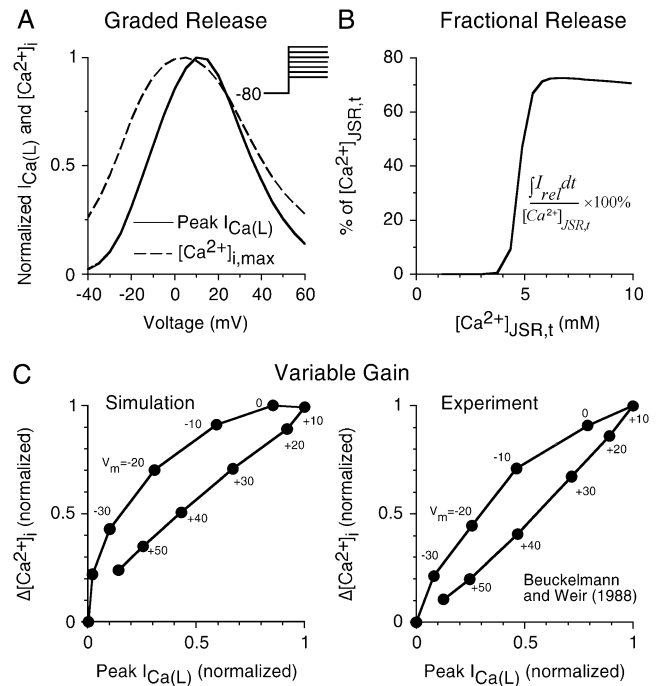

FIGURE 7 (*A*) Graded release of SR Ca^{2+}. In the simulation, voltage is clamped from −80 mV to the test potential. The solid trace shows normalized peak $I_{Ca(L)}$ and the dashed trace shows normalized peak $[Ca^{2+}]_i$. (*B*) Fractional SR release as a function of SR content. $[Ca^{2+}]_{JSR}$ is clamped at each value for 20 s. to allow RyR states to reach a new equilibrium, then the clamp is removed and a stimulus is applied. $[Ca^{2+}]_{JSR,t}$ is total JSR Ca^{2+} (free + Ca^{2+} bound CASQ2) and $\int I_{rel} dt$ is integrated over the interval from the time of stimulus to the peak of the CaT. (*C*) Voltage-dependent variable gain of SR Ca^{2+} release. The right panel shows experimentally measured dependence of $\Delta[Ca^{2+}]_i$ (difference between the peak $[Ca^{2+}]_i$ and resting $[Ca^{2+}]_i$) on $I_{Ca(L)}$ for different V_m values (indicated on *curve*) in guinea pig ventricular myocytes (from Beuckelmann and Wier (57), with permission). The corresponding simulated data are shown in the left panel. Note that for the same amplitude of $I_{Ca(L)}$, a larger release occurs at negative potentials.

clear that for the same magnitude of $I_{Ca(L)}$ the amount of SR release is greater at negative potentials. At 0 mV, the gain of SR Ca^{2+} release is 15.4 as computed with the following formula $Gain = \int F_{rel} dt / \int F_{I_{Ca(L)}} dt$, where F_{rel} is the Ca^{2+} flux from the SR and $F_{I_{Ca(L)}}$ is the Ca^{2+} flux through $I_{Ca(L)}$, integrated over the period from the beginning of the voltage clamp to the peak of the CaT. This value for gain is comparable to values measured in rabbit (56) and canine (58).

$I_{Ca(L)}$ during the action potential

An essential property of the L-type Markov model is the ability to recreate measured $I_{Ca(L)}$ amplitude and morphology during the AP. Fig. 8 shows an experimentally measured $I_{Ca(L)}$ (nifedipine-sensitive current) (59) compared to a simulated $I_{Ca(L)}$ during the application of an identical AP clamp waveform (10 APs at 1 Hz). The experiment was conducted in a guinea pig ventricular myocyte at 37°C with SR Ca^{2+} release intact. Note that both the simulated and measured $I_{Ca(L)}$ exhibit a peak value of ~6 pA/pF, a period of rapid inactivation, and a current magnitude during the AP plateau of ~3 pA/pF.

Rate dependence of APD, [Na$^+$]$_i$, and [Ca^{2+}]$_i$

Fig. 9 A compares simulated AP and [Ca^{2+}]$_i$ transient during the AP to their experimental counterparts (60). For this comparison, the amplitudes of the AP and [Ca^{2+}]$_i$ are not provided in the experimental tracings because the measured AP and [Ca^{2+}]$_i$ are expressed as fluorescence ratios of the voltage-sensitive dye RH237 and Ca^{2+}-sensitive dye Rhod-2. However, important temporal relationships between the AP and the [Ca^{2+}]$_i$ transient are observed in both the simulation and experiment, including a 5-ms delay between the AP upstroke and the initiation of release, a 25-ms delay between the AP

upstroke and the time of peak [Ca^{2+}]$_i$ transient, and a time constant of decay of the [Ca^{2+}]$_i$ transient of ~150 ms.

Simulated changes to APD, [Na$^+$]$_i$, peak [Ca^{2+}]$_i$, and diastolic [Ca^{2+}]$_i$ as a function of rate are summarized in Fig. 9 B. APD adaptation (61), [Na$^+$]$_i$ accumulation (62), and the positive force-frequency relationship (increase in peak [Ca^{2+}]$_i$ with increasing rate) (62) are consistent with experimental comparisons made in a previous publication (32).

APD and [Ca^{2+}]$_i$ restitution

Fig. 10, A and B, show restitution properties of the myocyte model. The myocyte is paced at a constant cycle length until steady state. Then a premature stimulus is applied with a coupling interval DI (diastolic interval, $DI = 0$ is APD$_{90}$ of the last paced AP). Fig. 10 A shows the last paced beat ($CL = 500$) and five APs with the associated $I_{Ca(L)}$ and [Ca^{2+}]$_i$ for five DI values (50 ms, 150 ms, 250 ms, 350 ms, and 450 ms). Note that at DI = 50 ms a normal [Ca^{2+}]$_i$ transient fails to occur despite a large $I_{Ca(L)}$ (i.e., a large triggering source). Also, note that the CaT at DI = 450 ms is larger then the CaT generated at steady state at $CL = 500$ ms. This is because the DI + APD$_{90}$ is longer than the initial $CL = 500$ ms and the SR has had a longer time to fill and the RyR has had more time to recover from inactivation resulting in a larger release and CaT.
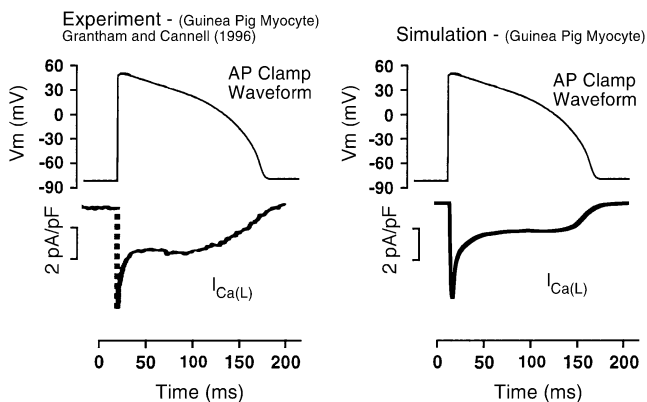

FIGURE 8 $I_{Ca(L)}$ during the action potential in the presence of SR Ca^{2+} release. The upper panels show the AP clamp waveform from Grantham and Cannell (59) used to generate the corresponding $I_{Ca(L)}$ (lower panels). The experimental $I_{Ca(L)}$ (nifedipine-sensitive current; lower left panel) is measured in guinea pig ventricular myocyte at 36°C. Experimental traces are reproduced from Grantham and Cannell (59), with permission.
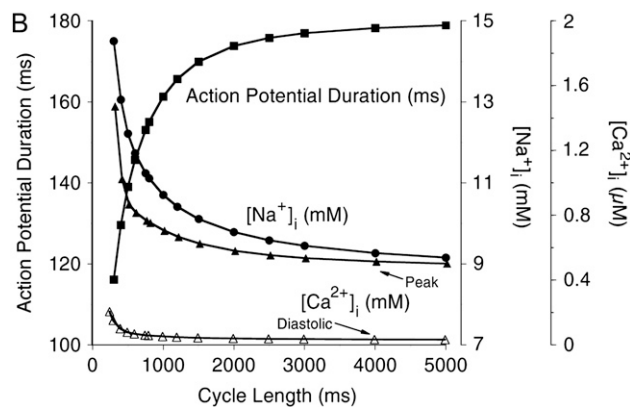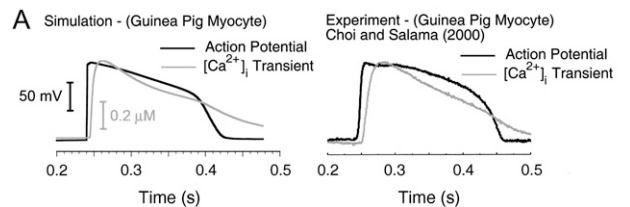

FIGURE 9   (A) Simulated AP and Ca^{2+} transient (left) compared to experimentally recorded AP and Ca^{2+} transient (right) in guinea pig ventricular myocyte at 37°C. The experiment is a simultaneous optical recording using the voltage-sensitive dye RH237 and Ca^{2+} sensitive indicator Rhod-2 (from Choi and Salama (60), with permission). (B) APD adaptation, [Na$^+$]$_i$ rate dependence, and [Ca^{2+}]$_i$ rate dependence. The figure shows the steady-state relationship (achieved after 5 min of pacing) between cycle length and APD (■). Corresponding changes in [Ca^{2+}]$_{i,max}$ (▲), [Ca^{2+}]$_{i,diastolic}$ (△), and [Na$^+$]$_i$ (●) are also shown.

Restitution data for three different pacing cycle lengths (CL = 1000 ms, 500 ms, and 300 ms) are shown in Fig. 10 B. At very short DI, dV/dt_{max} is slow due to incomplete recovery of I_{Na}. This results in decreased V_{max} and a larger driving force for $I_{Ca(L)}$, increasing the current at these short DIs. Although the triggering source is large (Peak $I_{Ca(L)}$), RyR channels remain inactivated preventing release. Only when RyR channels have recovered from inactivation does release occur. The duration of this interval where no SR release can occur is dependent on the pacing frequency (Peak RyR Open Probability and Peak I_{rel}). This phenomenon is related to recovery of SR Ca^{2+} content (63) and the relationship between bound CASQ2 and RyR recovery (46,63). At fast rates, the increased amount of Ca^{2+} in the cytosol ($\Delta[Ca^{2+}]_i$) leads to faster recovery of SR calcium content (Peak $[Ca^{2+}]_{JSR}$) and faster recovery of RyR and I_{rel} (Peak I_{rel}). At very long DI, it can be observed that the magnitude of I_{rel} is strongly dependent on SR content when Peak RyR Open Probability and Peak $I_{Ca(L)}$ are similar in magnitude for all three CLs.
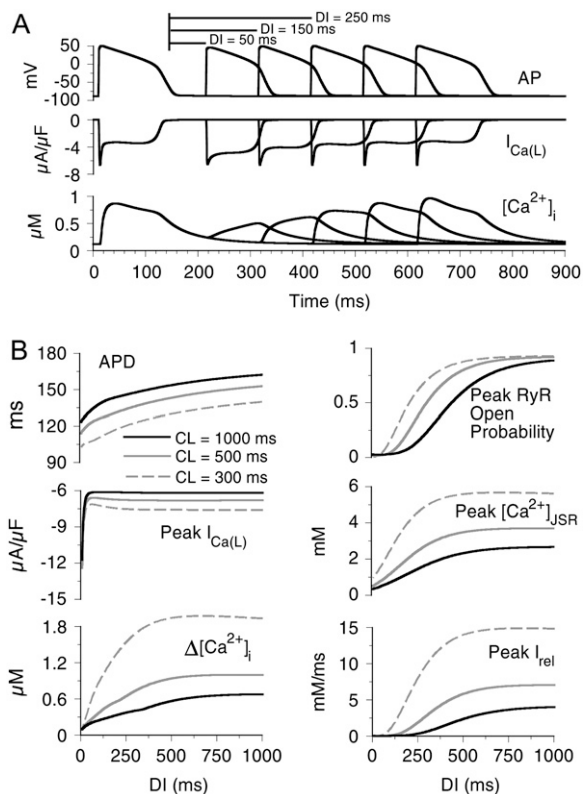

FIGURE 10 Restitution properties. The myocyte is paced at a constant cycle length for 5 min followed by a premature stimulus applied at varying diastolic intervals (*DI*). (*A*) Representative changes to AP, $I_{Ca(L)}$, and $[Ca^{2+}]_i$ for five different DIs (50 ms, 150 ms, 250 ms, 350 ms, and 450 ms) after pacing at CL = 500 ms. (*B*) Summary of restitution behavior for a myocyte paced at three different cycle lengths (CL = 300, 500, and 1000 ms). $\Delta[Ca^{2+}]_i$ is the difference between peak $[Ca^{2+}]_i$ and the $[Ca^{2+}]_i$ just before application of the premature stimulus.

Currents during the AP at fast and slow pacing

Steady-state AP, $[Ca^{2+}]_i$, $[Ca^{2+}]_{ss}$, and the significant currents that determine APD and AP morphology are shown in Fig. 11 for two different pacing frequencies. At rapid rate (CL = 300 ms, *gray curve*) $I_{Ca(L)}$ exhibits a larger peak and plateau compared to slow rate (CL = 1000 ms, *black curve*) (*B*). Although there is a greater CDI at CL = 300 ms due to the larger Ca^{2+} transient, the lower AP plateau increases the driving force for $I_{Ca(L)}$, resulting in a larger current. The lower plateau and shortened APD (*A*) are mostly due to the large I_{Ks} current that accumulates at fast rate (*F*).

The Na^+-Ca^{2+} exchanger within the subspace ($I_{NaCa,ss}$; *D*) provides little triggering Ca^{2+} compared to that provided by $I_{Ca(L)}$ and upon release of Ca^{2+} from the SR (and the subsequent increase in subspace Ca^{2+}) quickly shifts to the forward mode to remove Ca^{2+}. At fast rates when $[Ca^{2+}]_{ss}$ (*H*) is elevated, $I_{NaCa,ss}$ remains in the forward mode during most of the AP plateau.

L-type Ca^{2+} channel state residencies during the AP

The time course of L-type Ca^{2+} channel state residencies during the AP at fast and slow rates is shown in Fig. 12 (see Fig. 1 for the state diagram of the channel). At the slow rate (CL = 1000 ms, *black curve*), almost all the channels are able to fully recover to the closed states in ModeV (Fig. 12 *B*) before the pacing stimulus, whereas at the rapid rate (CL = 300 ms, *gray curve*) ~15% of the channels are still in ModeCa at the time of stimulus (Fig. 12, *B* and *G*, *arrows*). Despite a greater number of channels locked in ModeCa, the magnitude of $I_{Ca(L)}$ is larger at rapid rate due to the reduced V_m and increase in driving force. Upon depolarization, channels quickly move to the open state (Fig. 12 *C*). From the open state, channels inactivate via either fast VDI (I_{Vf}, Fig. 12 *D*) or slow VDI (I_{Vs}, Fig. 12 *E*). Upon the initiation of SR Ca^{2+} release, channels transition from ModeV to ModeCa and inactivate by CDI (Fig. 12, *G–J*); I_{VfCa} and I_{VsCa} contain channels that have inactivated via both VDI and CDI.

At rapid rate, a greater percentage of channels become inactivated by CDI due to the elevated $[Ca^{2+}]_i$. For the rapid rate, at t =100 ms after the time of stimulus, ~10% of the channels are inactivated solely by CDI, 40% solely by VDI, and 40% via both CDI and VDI. This is compared to 5%, 55%, and 30%, respectively, at the slow rate. The remaining 10% of channels are in either the closed or open states.

RyR channel state residencies during the AP

The time course of RyR channel state residencies during the AP at fast (CL = 300 ms, *gray curve*) and slow rate (CL = 1000 ms, *black curve*) is shown in Fig. 13 (see Fig. 2 *B* for the state diagram of RyR). Upon depolarization and elevation of $[Ca^{2+}]_{ss}$ by Ca^{2+} entry via $I_{Ca(L)}$, channels
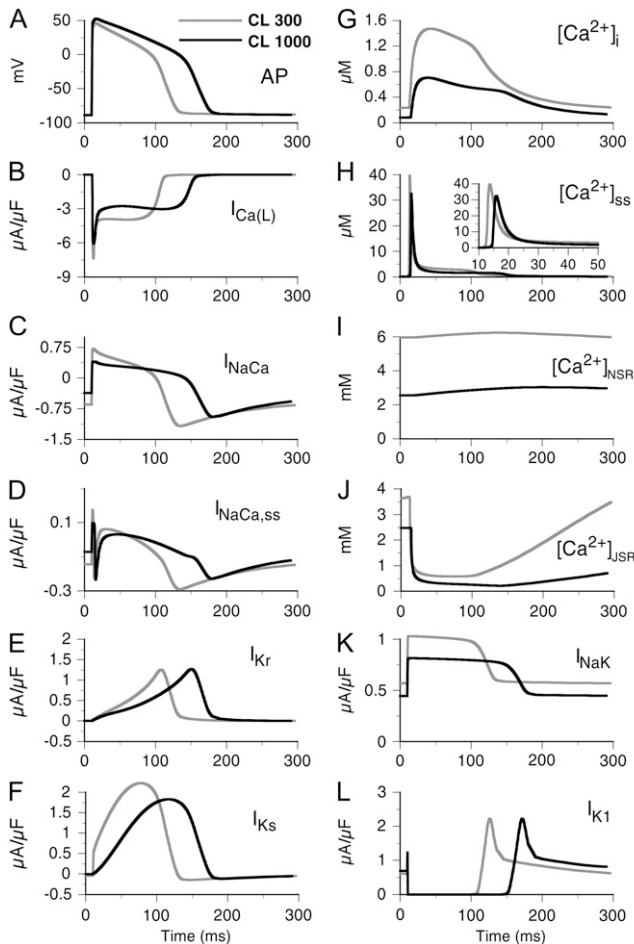
FIGURE 11   Action potential (*AP*), calcium transient ([Ca^{2+}]$_i$), I$_{Ca(L)}$, subspace calcium transient ([Ca^{2+}]$_{ss}$), I$_{NaCa}$, I$_{NaK}$, I$_{NaCa,ss}$, I$_{K1}$, I$_{Kr}$, and I$_{Ks}$ for two different pacing frequencies, *CL* = 1000 ms (*black curve*) and *CL* = 300 ms (*gray curve*).
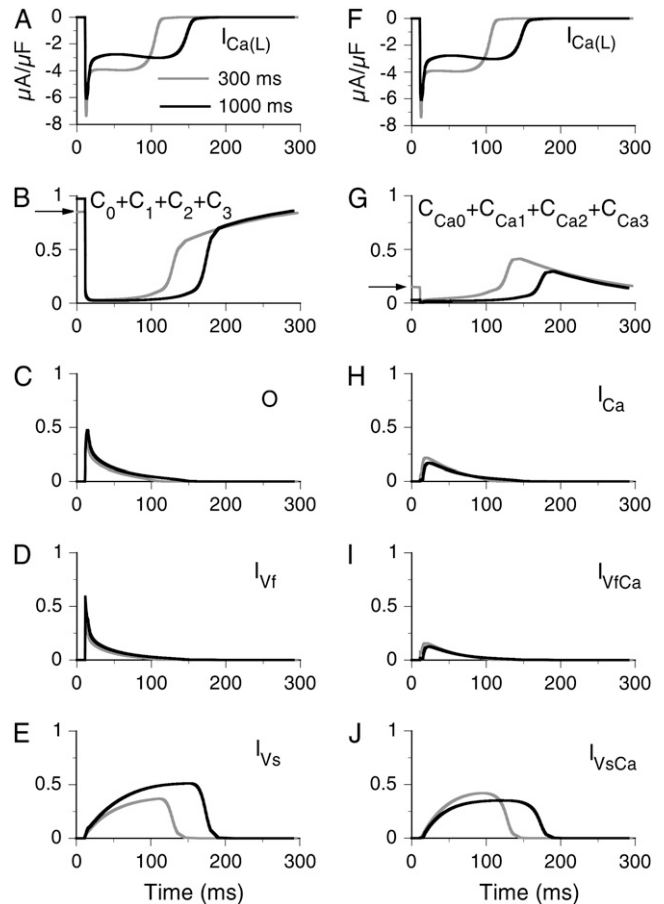

FIGURE 12   State residencies of the L-type Ca^{2+} channel during the time course of the action potential for two different pacing frequencies, *CL* = 1000 ms (*black curve*) and *CL* = 300 ms (*gray curve*). For identification of the channel states, refer to Fig. 1.

move rapidly from the closed state (Fig. 13 *D*) to the open state (Fig. 13 *C*) (Ca^{2+}-dependent activation). Channels then transition into the near inactivated states (I$_4$ and I$_5$, Fig. 13 *F*) due to the high concentration of Ca^{2+} in the subspace following SR release (Ca^{2+}-dependent inactivation). After AP repolarization, channels move from inactivated states I$_4$ and I$_5$ to I$_1$, I$_2$, and I$_3$ (Fig. 13, *F* and *E*) as subspace Ca^{2+} decreases. From I$_1$, I$_2$, and I$_3$, channels then recover to the closed states (Fig. 13 *D*) as the SR stores recover. This recovery from inactivated to closed states is dependent on the concentration of Ca^{2+} bound CASQ2. As can be seen in Fig. 13 *D*, the delay of recovery from inactivation is longer at slow rates than at fast rates. This is due to increased Ca^{2+} loading of the myocyte at rapid rate, which allows faster recovery of Ca^{2+}-bound CASQ2 and, in turn, faster recovery of RyR from inactivation after AP repolarization.

It can be observed that the RyR open probability (Fig. 13 *C*) at rapid rate is smaller than that at slow rate, but the maximum SR Ca^{2+} flux is greater (Fig. 13 *B*). The reason for

the decreased open probability is that 55% of the channels remain inactivated at rapid rate (Fig. 13 *E*, *arrow*), primarily due to the decreased time for recovery between beats. Despite the decreased open probability, I$_{rel}$ is larger due to the larger SR Ca^{2+} stores ([Ca^{2+}]$_{JSR}$) that result from rapid pacing (see Fig. 11 *J*). Increased [Ca^{2+}]$_{ss}$ (Fig. 11 *H*) at rapid rate (due to increased I$_{rel}$, Fig. 13 *B*) increases the percentage of RyR channels that are activated by Ca^{2+} (rightward transition on the state diagram) and the percentage of channels that are inactivated by Ca^{2+} (upward transition on the state diagram). Hence, at rapid rate more channels reside in I$_4$ and I$_5$ compared to slow rate (Fig. 13 *F*).

Timothy syndrome and loss of Ca$_V$1.2 VDI

The Ca$_V$1.2 mutation G406R, linked to the Timonthy syndrome, almost completely removes VDI of I$_{Ca(L)}$. In Fig. 14 *A* we show steady-state inactivation curves of I$_{Ca(L)}$ for the control model (*black trace*) and for G406R (*gray trace*) compared to experimentally measured values (*symbols*). Analysis of mRNA in heart and brain tissue by Splawski
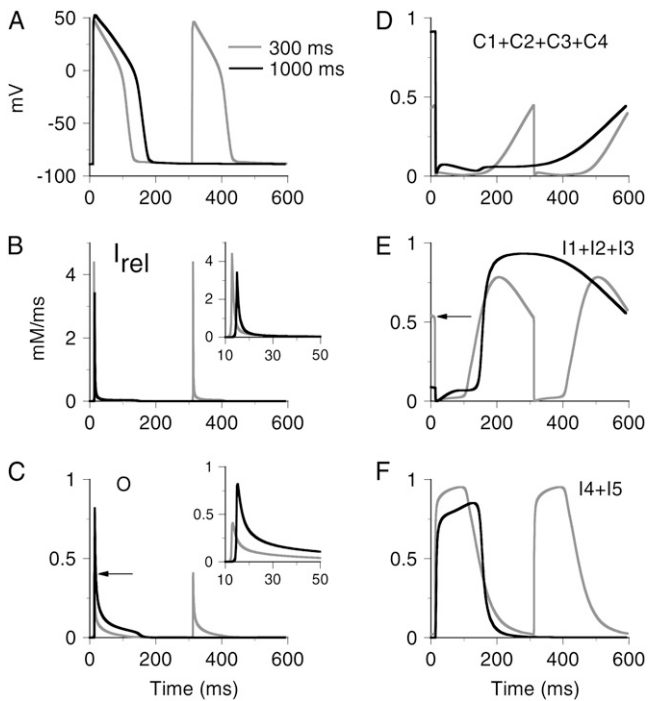
FIGURE 13   State residencies of the RyR channel during the time course of the action potential for two different pacing frequencies, $CL = 1000$ ms (*black curve*) and $CL = 300$ ms (*gray curve*). For identification of the channel states, refer to Fig. 2 *B*.

FIGURE 14   (*A*) Steady-state voltage-dependent inactivation curves of $Ca_V1.2$ for wild-type (*WT, black*) and mutation G406R (*gray*). The experimental data (*symbols*) (from Splawski et al. (13), with permission) were recorded in the absence of Ca^{2+}. (*B*) Steady-state APs at $CL = 1000$ ms for WT myocyte (*black trace*), a myocyte with 11.5% G406R channels (*dashed trace*), and with 23% G406R channels (*gray trace*). (*C*) Corresponding $I_{Ca(L)}$ (*arrow* indicates peak of $I_{Ca(L)}$ for WT) and (*D*) calcium transient, CaT.

et al. (13) showed that ∼23% of $Ca_V1.2$ channels contain the exon 8A in which the mutation G406R occurs. For this reason we show AP (Fig. 14 *B*), $I_{Ca(L)}$ (*C*), and CaT (*D*) for three scenarios—wild-type (*WT, black traces*), heterozygous expression (11.5% G406R $Ca_V1.2$ channels, *dashed gray traces*), and homozygous (23% G406R $Ca_V1.2$ channels, *gray traces*). The G406R mutation results in $I_{Ca(L)}$ current with a larger peak (Fig. 14 *C, arrow*) due to the loss of fast VDI. Recovery of current during the late phase of the AP corresponds with the decline of the CaT. This recovery from CDI results in an increased depolarizing $I_{Ca(L)}$ current that prolongs APD (clinically observed as prolongation of QT interval on the ECG) and increases myocyte Ca^{2+}. The increase of $[Ca^{2+}]_i$ results from both increased Ca^{2+} entry via $I_{Ca(L)}$ and reduced diastolic interval, a time during which excess Ca^{2+} is removed by the Na^+-Ca^{2+} exchanger.

DISCUSSION

In this study we present detailed kinetic models of $Ca_V1.2$ and RyR that interact within a subcellular restricted space. These models were incorporated into the LRd model of the mammalian ventricular cell with the following results: 1), The model of $Ca_V1.2$ reproduces experimental single channel data (mean open time, latency to first opening) and macroscopic current data (VDI, CDI, recovery from inactivation, $I_{Ca(L)}$ during the AP). 2), The $Ca_V1.2$-RyR interaction in the
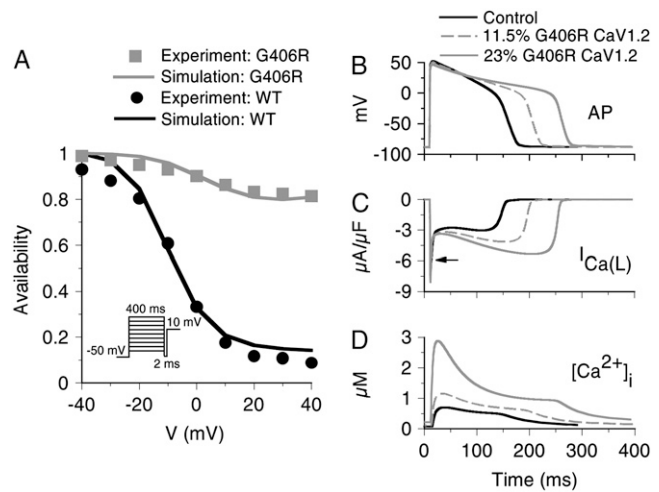
subspace reproduces graded SR Ca^{2+} release and voltage-dependent variable gain of release. 3), The model accurately reproduces adaptation of APD to changes in rate, rate dependence of $[Na^+]_i$ and the Ca^{2+} transient (force-frequency relationship), and restitution properties of APD and the Ca^{2+} transient during premature stimuli. 4), CDI of $Ca_V1.2$ is sensitive to Ca^{2+} that enters the subspace from L-type Ca^{2+} channels and from SR release. The relative contributions of these Ca^{2+} sources to total CDI vary with time after depolarization, with transition from early SR Ca^{2+} dominance to late L-type Ca^{2+} dominance, as seen experimentally. 5), The relative contribution of CDI to total inactivation of $I_{Ca(L)}$ is greater at negative potentials when VDI is weak. 6), CDI is greater at rapid rates due to elevated subspace Ca^{2+}. 7), Suppression of VDI due to the $Ca_V1.2$ mutation G406R results in APD prolongation and increased $[Ca^{2+}]_i$.

Divalent cations and $I_{Ca(L)}$ inactivation

In the $I_{Ca(L)}$ model development we utilized extensive experimental data obtained with divalent cations other than Ca^{2+} (i.e., Ba^{2+}, Mg^{2+}, Sr^{2+}, Cd^{2+}) as the charge carrier to eliminate CDI. There has been some evidence to indicate that these substitutions (specifically Ba^{2+}) for Ca^{2+} may also cause some inactivation of the channel (64). The mechanism by which other divalent cations cause inactivation is not known. Making the assumption that divalent cations other than Ca^{2+} can be used to indicate pure VDI can lead to an overestimation of the magnitude of VDI compared to CDI. To avoid this potential pitfall, studies of VDI have been

conducted utilizing monovalent cations as the charge carrier (65,66). However, in these studies isoproternol (ISO) was used to amplify the current for facilitation of measurement. In experiments conducted by Findlay in the absence of ISO (67), the current through I$_{Ca(L)}$ carried by Ba^{2+}, Sr^{2+}, and Na$^+$ all exhibited similar inactivation kinetics, implying that Ba^{2+} and other divalent cations are suitable substitutes for determining VDI when ISO is absent. All simulations in this study were conducted under such basal conditions, in the absence of β-adrenergic effects.

I$_{Ca(L)}$: Ca^{2+} versus voltage dependent inactivation

There has been some debate as to which mechanism dominates inactivation of L-type Ca^{2+} channels, VDI, or CDI. In our simulations, we show that in the absence of CDI, VDI can cause >80% inactivation of the current (Fig. 3 B) for voltage clamps to positive potentials. Experimental data of steady-state inactivation from Linz and Meyer (66) show that in the absence of CDI only 50% of the channels are inactivated due to VDI for voltage clamps to positive potentials. The primary reason for differences between our simulation and the Linz and Meyer experiments is their use of ISO in the solution. In a series of studies (51,67–69), Findlay demonstrated that when β-adrenergic stimulation effects were induced by the addition of ISO to the bath solution, the contribution of VDI to total inactivation was greatly reduced and CDI became dominant. Findlay proposed a ''switch'' whereby phosphorylation of the channel turns off rapid VDI and CDI becomes dominant (55). Our simulations are conducted in the absence of β-adrenergic stimulation and are in agreement with Findlay experiments conducted in the absence of ISO. In Fig. 6, A and B, we show that the relative contributions of CDI and VDI to total inactivation are both voltage and time dependent. We also show that the relative contribution of CDI and VDI to total inactivation is rate dependent (Fig. 12); specifically the contribution of CDI to total inactivation increases with increased rate due to the elevation of total [Ca^{2+}] within the myocyte. Loss of VDI, as shown in simulations of the Ca$_V$1.2 mutation G406R (Fig. 14), leads to APD prolongation and an increase in [Ca^{2+}]$_i$. It is clear that both VDI and CDI are important mechanisms of I$_{Ca(L)}$ inactivation. The loss of either of these mechanisms of inactivation can lead to APD prolongation and calcium overload, resulting in increased susceptibility to arrhythmia.

It has been well established that CDI of I$_{Ca(L)}$ occurs by Ca^{2+} binding to a constitutively bound calmodulin molecule on the C-terminus of the Ca$_V$1.2 α_1 subunit (22,23,70). But there has been some evidence that Ca^{2+} in the pore of the channel or Ca^{2+} very near the channel pore can also cause CDI (71). We formulated CDI as a function of both I$_{Ca(L)}$ (representing Ca^{2+} passing through the channel pore) and [Ca^{2+}]$_{ss}$ (Ca^{2+} that can bind to the C-terminus inactivation site). However, extensive experimental data were fitted by the model with CDI dependence on [Ca^{2+}]$_{ss}$ alone, sug-

gesting a minor role for pore Ca^{2+} compared to subspace Ca^{2+} in I$_{Ca(L)}$ inactivation.

I$_{Ca(L)}$ selectivity filter

The L-type Ca^{2+} channel is permeable to both monovalent and divalent cations, but there has been some evidence to suggest that when Ca^{2+} is present, the channel is selective almost exclusively for Ca^{2+} and does not allow passage of other ions (72,73). In our model of I$_{Ca(L)}$ the channel is permeable to Ca^{2+}, K$^+$, and Na$^+$ with membrane permeabilities of 1.215×10^{-3} cm/s, 4.34×10^{-7} cm/s, and 1.515×10^{-6} cm/s, respectively. We conducted simulations where the permeability of Na$^+$ and K$^+$ through I$_{Ca(L)}$ was eliminated but discovered that the resultant AP morphology did not fit experimentally recorded guinea pig APs.

I$_{Ca(L)}$ facilitation

L-type Ca^{2+} channels exhibit a property whereby the channel current magnitude increases with successive depolarizations. This property is known as facilitation and is thought to play a role in generating positive force frequency. I$_{Ca(L)}$ facilitation is not reproduced by the model presented here, but the model still exhibits a positive force frequency relationship due to [Ca^{2+}]$_i$ loading at fast rate. Recent experimental evidence has shown that I$_{Ca(L)}$ facilitation is a result of CaMKII activation (23,24,74–76). CaMKII is sensitive to frequency changes in [Ca^{2+}]$_i$ and when activated, can phosphorylate several targets including Ca$_V$1.2, SERCA, and RyRs. A recent model of the canine ventricular AP incorporated the CaMKII signaling pathways and its effects on the AP and Ca^{2+} transient (9). Modification of this signaling pathway for inclusion in the guinea pig myocyte model could be done in future development to incorporate I$_{Ca(L)}$ facilitation. I$_{Ca(L)}$ is also augmented by β-adrenergic stimulation (77). The simulations in this study are conducted under basal conditions in the absence of β-adrenergic effects. Models of the β-adrenergic signaling pathway (78) could also be adapted and incorporated in the cell model for studies of cellular behavior under various levels of β-adrenergic tone.

Gain and local control of SR Ca^{2+} release

Local control theory of SR Ca^{2+} release says that the individual discrete openings of single L-type Ca^{2+} channels signal the opening of nearby RyRs, the Ca^{2+} from which can recruit adjacent RyRs leading to SR release. This concept is important for understanding variable gain of SR release, where it is observed that for the same magnitude of I$_{Ca(L)}$, a larger release is achieved at negative potentials than at positive potentials. The idea is that at negative potentials fewer Ca$_V$1.2 channels open but because the driving force for Ca^{2+} is large, a large amount of Ca^{2+} enters through the open channels creating sufficient local Ca^{2+} levels to trigger

local RyR openings. At positive potentials, many more $Ca_V1.2$ channels will open, but the average current per channel will be low because of a small driving force. Consequently, at some sites $[Ca^{2+}]_{ss}$ is not large enough to trigger opening of local RyRs. There have been important modeling efforts to recreate local control of SR release at the level of these local interactions (17,18,79–81). The whole-cell model presented here uses a global formulation of I_{rel} to achieve graded response and variable gain. Using this macroscopic formulation, the model recreates behavior of $I_{Ca(L)}$, I_{rel}, and $[Ca^{2+}]_i$ that corresponds well to experimentally measured data at a variety of test potentials and pacing rates. This approach is computationally efficient and permits simulating cellular behavior over many beats of pacing and during AP propagation in the multicellular tissue, a property that is necessary for studying cardiac arrhythmias. However, microscopic details of local control dynamics are not represented explicitly in the model.

RyR Ca^{2+}-dependent inactivation and adaptation

The mechanism that terminates SR Ca^{2+} release is not fully understood and several possible control mechanisms have been proposed (16). There has been evidence that RyR channels do not undergo Ca^{2+}-dependent inactivation (82), contrary to the proposed RyR kinetic model presented here. Suggested mechanisms of SR release termination, such as stochastic attrition (83) (closure of RyR channels and their neighbors due to reduction of local Ca^{2+} as a result of spontaneous stochastic closure of local RyRs) and RyR adaptation (a decrease of RyR sensitivity to local Ca^{2+} following a Ca^{2+} stimulus, a process distinct from inactivation in that the channels can exhibit further opening following an additional, larger Ca^{2+} stimulus) cannot be replicated in this study without including a more detailed model of local control (17,18,84) and/or RyR kinetics (41,85). Another proposed mechanism of SR Ca^{2+} release termination is due to depletion of luminal Ca^{2+} (46,63,86). This mechanism is similar to the CASQ2-mediated recovery from inactivation in the model presented here. In our formulation, both cytosolic and luminal SR Ca^{2+} (via CASQ2) play an important role in RyR inactivation and RyR recovery from inactivation. Despite the lack of clarity concerning RyR inactivation and SR Ca^{2+} release termination, the RyR model presented here accurately recreates the time course and magnitude of SR Ca^{2+} release for a multitude of voltage clamp protocols and pacing frequencies necessary for validating the $Ca_V1.2$ model and its use in the simulations presented.

APPENDIX: MODEL EQUATIONS

L-type Ca^{2+} channel $I_{Ca(L)}$

$$\alpha = 0.925 \cdot \exp(V_m/30)$$

$$\beta = 0.39 \cdot \exp(-V_m/40)$$

$$\alpha_0 = 4 \cdot \alpha$$

$$\alpha_1 = 3 \cdot \alpha$$

$$\alpha_2 = 2 \cdot \alpha$$

$$\alpha_3 = \alpha$$

$$\beta_0 = \beta$$

$$\beta_1 = 2 \cdot \beta$$

$$\beta_2 = 3 \cdot \beta$$

$$\beta_3 = 4 \cdot \beta$$

$$\gamma_f = 0.245 \cdot \exp(V_m/10)$$

$$\gamma_s = 0.005 \cdot \exp(-V_m/40)$$

$$\phi_f = 0.02 \cdot \exp(V_m/500)$$

$$\phi_s = 0.03 \cdot \exp(-V_m/280)$$

$$\lambda_f = 0.035 \cdot \exp(-V_m/300)$$

$$\lambda_s = 0.0011 \cdot \exp(V_m/500)$$

$$\omega_f = (\beta_3 \cdot \lambda_f \cdot \gamma_f)/(\alpha_3 \cdot \phi_f)$$

$$\omega_s = (\beta_3 \cdot \lambda_s \cdot \gamma_s)/(\alpha_3 \cdot \phi_s)$$

$$\omega_{sf} = (\lambda_s \cdot \phi_f)/\lambda_f; \omega_{fs} = \phi_s$$

$$\delta = \frac{4}{1 + 1/[Ca^{2+}]_{ss}}$$

$$\theta = 0.01$$

$$\frac{dC_0}{dt} = C_1 \cdot \beta_0 + C_{0Ca} \cdot \theta - C_0 \cdot (\alpha_0 + \delta)$$

$$\frac{dC_1}{dt} = C_0 \cdot \alpha_0 + C_2 \cdot \beta_1 + C_{1Ca} \cdot \theta - C_1 \cdot (\alpha_1 + \beta_0 + \delta)$$

$$\frac{dC_2}{dt} = C_1 \cdot \alpha_1 + C_3 \cdot \beta_2 + C_{2Ca} \cdot \theta - C_2 \cdot (\alpha_2 + \beta_1 + \delta)$$

$$\frac{dC_3}{dt} = C_2 \cdot \alpha_2 + O \cdot \beta_3 + I_{Vf} \cdot \omega_f + I_{Vs} \cdot \omega_s$$
$$+ C_{3Ca} \cdot \theta - C_3 \cdot (\alpha_3 + \beta_2 + \gamma_f + \gamma_s + \delta)$$

$$\frac{dO}{dt} = C_3 \cdot \alpha_3 + I_{Vf} \cdot \lambda_f + I_{Vs} \cdot \lambda_s$$
$$+ I_{Ca} \cdot \theta - O \cdot (\beta_3 + \phi_f + \phi_s + \delta)$$

$$\frac{dI_{Vf}}{dt} = C_3 \cdot \gamma_f + O \cdot \phi_f + I_{Vs} \cdot \omega_{sf} + I_{VfCa} \cdot \theta$$
$$- I_{Vf} \cdot (\omega_f + \lambda_f + \omega_{fs} + \delta)$$

$$\frac{dI_{Vs}}{dt} = C_3 \cdot \gamma_s + O \cdot \phi_s + I_{Vf} \cdot \omega_{fs} + I_{VsCa} \cdot \theta$$
$$- I_{Vs} \cdot (\omega_s + \lambda_s + \omega_{sf} + \delta)$$

$$\frac{dC_{0Ca}}{dt} = C_{1Ca} \cdot \beta_0 + C_0 \cdot \delta - C_{0Ca} \cdot (\alpha_0 + \theta)$$

$$\frac{dC_{1Ca}}{dt} = C_{0Ca} \cdot \alpha_0 + C_{2Ca} \cdot \beta_1 + C_1 \cdot \delta - C_{1Ca} \cdot (\alpha_1 + \beta_0 + \theta)$$

$$\frac{dC_{2Ca}}{dt} = C_{1Ca} \cdot \alpha_1 + C_{3Ca} \cdot \beta_2 + C_2 \cdot \delta - C_{2Ca} \cdot (\alpha_2 + \beta_1 + \theta)$$

$$\frac{dC_{3Ca}}{dt} = C_{2Ca} \cdot \alpha_2 + I_{Ca} \cdot \beta_3 + I_{VfCa} \cdot \omega_f + I_{VsCa} \cdot \omega_s$$
$$+ C_3 \cdot \delta - C_{3Ca} \cdot (\alpha_3 + \beta_2 + \gamma_f + \gamma_s + \theta)$$

$$\frac{dI_{Ca}}{dt} = C_{3Ca} \cdot \alpha_3 + I_{VfCa} \cdot \lambda_f + I_{VsCa} \cdot \lambda_s + O \cdot \delta$$
$$- I_{Ca} \cdot (\beta_3 + \phi_f + \phi_s + \theta)$$

$$\frac{dI_{VfCa}}{dt} = C_{3Ca} \cdot \gamma_f + I_{Ca} \cdot \phi_f + I_{VsCa} \cdot \omega_{sf}$$
$$+ I_{Vf} \cdot \delta - I_{VfCa} \cdot (\omega_f + \lambda_f + \omega_{fs} + \theta)$$

$$\frac{dI_{VsCa}}{dt} = C_{3Ca} \cdot \gamma_s + I_{Ca} \cdot \phi_s + I_{VfCa} \cdot \omega_{fs} + I_{Vs} \cdot \delta$$
$$- I_{VsCa} \cdot (\omega_s + \lambda_s + \omega_{sf} + \theta)$$

I$_{rel}$

Rates of RyR activation and deactivation were increased from those based on lipid-bilayer studies in the original publication of Fill et al. (39) to account for differences in temperature and to create an SR flux that generates a time course and magnitude of the CaT that closely fit experimentally recorded values. For this reason, the rates were not increased uniformly. The activation rate α_{1R} was increased 3.5 times, and α_{2R}, α_{3R}, and α_{4R} were increased seven times. The deactivation rates β_{1R}, β_{2R}, and β_{3R} were increased five times and the deactivation rate β_{4R} was increased 25 times.

$$\alpha_{1R} = 1750 \cdot [Ca^{2+}]_{ss}$$

$$\alpha_{2R} = \alpha_{3R} = \alpha_{4R} = 5600 \cdot [Ca^{2+}]_{ss}$$

$$\beta_{1R} = 5$$

$$\beta_{2R} = 2.625$$

$$\beta_{3R} = 1$$

$$\beta_{4R} = 6.25$$

$$\gamma_{1R} = 0.4 \cdot [Ca^{2+}]_{ss}$$

$$\bar{I}_{Ca} = P_{Ca} \cdot z_{Ca}^2 \cdot \frac{V_m \cdot F^2}{RT} \cdot \frac{\gamma_{Cai} \cdot [Ca^{2+}]_{ss} \cdot \exp((z_{Ca} \cdot V_m \cdot F)/(RT)) - \gamma_{Cao} \cdot [Ca^{2+}]_o}{\exp((z_{Ca} \cdot V_m \cdot F)/(RT)) - 1}$$

$$P_{Ca} = 0.001215; \gamma_{Cai} = 0.01; \gamma_{Cao} = 0.341$$

$$\gamma_{2R} = 1.2 \cdot [Ca^{2+}]_{ss}$$

$$\bar{I}_{Ca,Na} = P_{Na} \cdot z_{Na} \cdot \frac{V_m \cdot F^2}{RT} \cdot \frac{\gamma_{Nai} \cdot [Na^+]_{ss} \cdot \exp((z_{Na} \cdot V_m \cdot F)/(RT)) - \gamma_{Nao} \cdot [Na^+]_o}{\exp((z_{Na} \cdot V_m \cdot F)/(RT)) - 1}$$

$$P_{Na} = 1.518 \times 10^{-6}; \gamma_{Nai} = 0.75; \gamma_{Nao} = 0.75$$

$$\gamma_{3R} = 2.8 \cdot [Ca^{2+}]_{ss}$$

$$\bar{I}_{Ca,K} = P_K \cdot z_K \cdot \frac{V_m \cdot F^2}{RT} \cdot \frac{\gamma_{Ki} \cdot [K^+]_{ss} \cdot \exp((z_K \cdot V_m \cdot F)/(RT)) - \gamma_{Ko} \cdot [K^+]_o}{\exp((z_K \cdot V_m \cdot F)/(RT)) - 1}$$

$$P_K = 4.34 \times 10^{-7}; \gamma_{Ki} = 0.75; \gamma_{Ko} = 0.75$$

$$I_{Ca(L)} = \bar{I}_{Ca} \cdot O$$

$$I_{Ca,Na} = \bar{I}_{Ca,Na} \cdot O.$$

$$I_{Ca,K} = \bar{I}_{Ca,K} \cdot O.$$

$$\gamma_{4R} = 5.2 \cdot [Ca^{2+}]_{ss}$$
$$\gamma_{5R} = 8.4 \cdot [Ca^{2+}]_{ss}$$
$$\delta_{1R} = \frac{0.01}{1 + (\overline{[csqn]} \cdot 0.75/[csqn])^9}$$
$$\delta_{2R} = \delta_{1R}/10$$
$$\delta_{3R} = \delta_{1R}/100$$
$$\delta_{4R} = \delta_{1R}/1000$$
$$\delta_{5R} = \delta_{1R}/10000$$

$$\frac{dC_1}{dt} = C_2 \cdot \beta_{1R} + I_1 \cdot \delta_{1R} - C_1 \cdot (\alpha_{1R} + \gamma_{1R})$$

$$\frac{dC_2}{dt} = C_1 \cdot \alpha_{1R} + C_3 \cdot \beta_{2R} + I_2 \cdot \delta_{2R} - C_2 \cdot (\beta_{1R} + \alpha_{2R} + \gamma_{2R})$$

$$\frac{dC_3}{dt} = C_2 \cdot \alpha_{2R} + C_4 \cdot \beta_{3R} + I_3 \cdot \delta_{3R} - C_3 \cdot (\beta_{2R} + \alpha_{3R} + \gamma_{3R})$$

$$\frac{dC_4}{dt} = C_3 \cdot \alpha_{3R} + O \cdot \beta_{4R} + I_4 \cdot \delta_{4R} - C_4 \cdot (\beta_{3R} + \alpha_{4R} + \gamma_{4R})$$

$$\frac{dO}{dt} = C_4 \cdot \alpha_{4R} + I_5 \cdot \delta_{5R} - O \cdot (\beta_{4R} + \gamma_{5R})$$

$$\frac{dI_1}{dt} = I_2 \cdot \beta_{1R} + C_1 \cdot \gamma_{1R} - I_1 \cdot (\alpha_{1R} + \delta_{1R})$$

$$\frac{dI_2}{dt} = I_1 \cdot \alpha_{1R} + I_3 \cdot \beta_{2R} + C_2 \cdot \gamma_{2R} - I_2 \cdot (\beta_{1R} + \alpha_{2R} + \delta_{2R})$$

$$\frac{dI_3}{dt} = I_2 \cdot \alpha_{2R} + I_4 \cdot \beta_{3R} + C_3 \cdot \gamma_{3R} - I_3 \cdot (\beta_{2R} + \alpha_{3R} + \delta_{3R})$$

$$\frac{dI_4}{dt} = I_3 \cdot \alpha_{3R} + I_5 \cdot \beta_{4R} + C_4 \cdot \gamma_{4R} - I_4 \cdot (\beta_{3R} + \alpha_{4R} + \delta_{4R})$$

$$\frac{dI_5}{dt} = I_4 \cdot \alpha_{4R} + O \cdot \gamma_{5R} - I_5 \cdot (\beta_{4R} + \delta_{5R})$$

$$gradedrel = \frac{1}{1 + \exp\left(\frac{20 + I_{Ca(L)}}{6}\right)} - 0.034445$$

$$vgainofrel = 1 + \exp\left(\frac{0.015 \cdot \bar{I}_{Ca} + 1.25}{0.75}\right)$$

$$\tau_b = 3.7 + \frac{6.1}{1 + \exp\left(\frac{V_m + 25}{4.5}\right)}$$

$$g_\infty = \frac{1}{1 + \exp\left(\frac{V_m + 60}{5.6}\right)}$$

If $V_m \le 0\,\text{mV}$,

$$\tau_g = -0.875 \cdot V_m + 12,$$

else

$$\tau_g = 12$$

$$I_{Ca(T)} = \bar{G}_{Ca(T)} \cdot b \cdot g \cdot (V_m - E_{Ca}).$$

I$_{Ks}$

$$\bar{G}_{Ks} = 0.3031 \cdot \left(1 + \frac{0.6}{1 + (3.8 \times 10^{-5}/[Ca^{2+}]_i)^{1.4}}\right)$$

$$E_{Ks} = \frac{R \cdot T}{F} \cdot \ln\left(\frac{[K^+]_o + P_{Na,k} \cdot [Na^+]_o}{[K^+]_i + P_{Na,k} \cdot [Na^+]_i}\right)$$

$$X_{s\infty} = X_{s2\infty} = \frac{1}{1 + \exp\left(\frac{1.5 - V_m}{16.7}\right)}$$

$$\tau_{xs1} = \frac{1}{\frac{7.19 \times 10^{-5} \cdot (V_m + 30)}{1 - \exp(-0.148 \cdot (V_m + 30))} + \frac{1.31 \times 10^{-4} \cdot (V_m + 30)}{\exp(0.0687 \cdot (V_m + 30)) - 1}}$$

$$G_{rel} = 250 \cdot \frac{gradedrel}{vgainofrel}$$

$$I_{rel} = G_{rel} \cdot O \cdot ([Ca^{2+}]_{JSR} - [Ca^{2+}]_{ss}).$$

$$\tau_{xs2} = 4 \cdot \tau_{xs1}$$

$$P_{Na,K} = 0.01833$$

$$I_{Ks} = \bar{G}_{Ks} \cdot X_s \cdot X_{s2} \cdot (V_m - E_{Ks}).$$

I$_{Ca(T)}$

$$\bar{G}_{Ca(T)} = 0.005$$

$$E_{Ca} = \frac{R \cdot T}{2 \cdot F} \cdot \ln\left(\frac{[Ca^{2+}]_o}{[Ca^{2+}]_i}\right)$$

$$b_\infty = \frac{1}{1 + \exp\left(\frac{14.0 - V_m}{10.8}\right)}$$

I$_{Kr}$

$$\bar{G}_{Kr} = 0.031368 \cdot \sqrt{\frac{[K^+]_o}{5.4}}$$

$$E_{Ks} = \frac{R \cdot T}{F} \cdot \ln\left(\frac{[K^+]_o}{[K^+]_i}\right)$$

$$X_{r\infty} = \frac{1}{1 + \exp\left(\frac{-(V_m + 10.085)}{4.25}\right)}$$

$$\tau_{xr} = \cfrac{1}{\cfrac{1.38 \times 10^{-3} \cdot (V_m + 14.2)}{1 - \exp(-0.123 \cdot (V_m + 14.2))} + \cfrac{6.1 \times 10^{-4} \cdot (V_m + 38.9)}{\exp(0.145 \cdot (V_m + 38.0)) - 1}}$$

$$R_{Kr} = \cfrac{1}{1 + \exp\left(\cfrac{V_m + 9}{18.4}\right)}$$

$$I_{Kr} = \overline{G}_{Kr} \cdot X_r \cdot R_{Kr} \cdot (V_m - E_{Kr}).$$

$$\beta_h = \cfrac{1}{0.13 \cdot \left(1 + \exp\left(\cfrac{V_m + 10.66}{-11.1}\right)\right)}$$

$$\alpha_j = 0.0$$

$$\beta_j = \cfrac{0.3 \cdot \exp(-2.535 \times 10^{-7} \cdot V_m)}{1 + \exp(-0.1 \cdot (V_m + 32))},$$

I$_{NaCa}$ & I$_{NaCa,ss}$

$$I_{NaCa} = \cfrac{0.8 \cdot c_1 \cdot \exp\left(\cfrac{(\gamma - 1) \cdot V_m \cdot F}{R \cdot T}\right) \cdot \left(\exp\left(\cfrac{V_m \cdot F}{R \cdot T}\right) \cdot [Na^+]_i^3 \cdot [Ca^{2+}]_o - c_3 \cdot [Na^+]_o^3 \cdot [Ca^{2+}]_i\right)}{1 + c_2 \cdot \exp\left(\cfrac{(\gamma - 1) \cdot V_m \cdot F}{R \cdot T}\right) \cdot \left(\exp\left(\cfrac{V_m \cdot F}{R \cdot T}\right) \cdot [Na^+]_i^3 \cdot [Ca^{2+}]_o + c_3 \cdot [Na^+]_o^3 \cdot [Ca^{2+}]_i\right)}$$

$$I_{NaCa,ss} = \cfrac{0.2 \cdot c_1 \cdot \exp\left(\cfrac{(\gamma - 1) \cdot V_m \cdot F}{R \cdot T}\right) \cdot \left(\exp\left(\cfrac{V_m \cdot F}{R \cdot T}\right) \cdot [Na^+]_{ss}^3 \cdot [Ca^{2+}]_o - c_3 \cdot [Na^+]_o^3 \cdot [Ca^{2+}]_{ss}\right)}{1 + c_2 \cdot \exp\left(\cfrac{(\gamma - 1) \cdot V_m \cdot F}{R \cdot T}\right) \cdot \left(\exp\left(\cfrac{V_m \cdot F}{R \cdot T}\right) \cdot [Na^+]_{ss}^3 \cdot [Ca^{2+}]_o + c_3 \cdot [Na^+]_o^3 \cdot [Ca^{2+}]_{ss}\right)}$$

$$\gamma = 0.15; c_1 = 0.000225; c_2 = 0.0001; c_3 = 1.5.$$

If $V_m < -40$ mV

$$\alpha_h = 0.135 \cdot \exp\left(\cfrac{(80 + V_m)}{-6.8}\right)$$

I$_{Na}$

$$\overline{G}_{Na} = 16$$

$$\beta_h = 3.56 \cdot \exp(0.079 \cdot V_m) + 3.1 \times 10^5 \cdot \exp(0.35 \cdot V_m)$$

$$\alpha_j = \cfrac{(-1.2714 \times 10^5 \cdot \exp(0.2444 \cdot V_m) - 3.474 \times 10^{-5} \cdot \exp(-0.04391 \cdot V_m)) \cdot (V_m + 37.78)}{1 + \exp(0.311 \cdot (V_m + 79.23))}$$

$$E_{Na} = \cfrac{RT}{F} \cdot \ln\left(\cfrac{[Na^+]_o}{[Na^+]_i}\right)$$

$$\alpha_m = 0.32 \cdot \cfrac{(V_m + 47.13)}{1 - \exp(-0.1 \cdot (V_m + 47.13))}$$

$$\beta_m = 0.08 \cdot \exp\left(\cfrac{-V_m}{11}\right)$$

If $V_m \geq -40\,mV$,

$$\alpha_h = 0.0$$

$$\beta_j = \cfrac{0.1212 \cdot \exp(-0.01052 \cdot V_m)}{1 + \exp(-0.1378 \cdot (V_m + 40.14))}$$

$$I_{Na} = \overline{G}_{Na} \cdot m^3 \cdot h \cdot j \cdot (V_m - E_{Na}).$$

Time-independent currents

I$_{Ca,b}$

$$\overline{G}_{Ca,b} = 0.003016$$

$$E_{\mathrm{Ca,b}} = \frac{RT}{F \cdot z_{\mathrm{ca}}} \cdot \ln\left(\frac{[Ca^{2+}]_{\mathrm{o}}}{[Ca^{2+}]_{\mathrm{i}}}\right)$$

$$I_{\mathrm{Ca,b}} = \overline{G}_{\mathrm{Ca,b}} \cdot (V_{\mathrm{m}} - E_{\mathrm{Ca,b}}).$$

$I_{Na,b}$

$$\overline{G}_{\mathrm{Na,b}} = 0.0002$$

$$E_{\mathrm{Na,b}} = \frac{RT}{F} \cdot \ln\left(\frac{[Na^+]_{\mathrm{o}}}{[Na^+]_{\mathrm{i}}}\right)$$

$$I_{\mathrm{Na,b}} = \overline{G}_{\mathrm{Na,b}} \cdot (V_{\mathrm{m}} - E_{\mathrm{Na,b}}).$$

I_{Kp}

$$\overline{G}_{\mathrm{Kp}} = 5.52 \times 10^{-4}$$

$$E_{\mathrm{Kp}} = \frac{RT}{F} \cdot \ln\left(\frac{[K^+]_{\mathrm{o}}}{[K^+]_{\mathrm{i}}}\right)$$

$$K_{\mathrm{p}} = \frac{1}{1 + \exp\left(\dfrac{7.488 - V_{\mathrm{m}}}{5.98}\right)}$$

$$I_{\mathrm{Kp}} = \overline{G}_{\mathrm{Kp}} \cdot K_{\mathrm{p}} \cdot (V_{\mathrm{m}} - E_{\mathrm{Kp}}).$$

I_{NaK}

$$\overline{G}_{\mathrm{NaK}} = 2.25$$

$$\sigma = \frac{\exp([Na^+]_{\mathrm{o}}/67.3) - 1}{7}$$

$$f_{\mathrm{NaK}} = \frac{1}{1 + 0.1245 \cdot \exp\left(\dfrac{-0.1 \cdot V_{\mathrm{m}} \cdot F}{RT}\right) + 0.0365 \cdot \sigma \cdot \exp\left(\dfrac{-V_{\mathrm{m}} \cdot F}{RT}\right)}$$

$$K_{\mathrm{m,Nai}} = 10; K_{\mathrm{m,Ko}} = 1.5$$

$$I_{\mathrm{NaK}} = \overline{G}_{\mathrm{NaK}} \cdot \frac{f_{\mathrm{NaK}}}{1 + \left(\dfrac{K_{\mathrm{m,Nai}}}{[Na^+]_{\mathrm{i}}}\right)^2} \cdot \left(\frac{[K^+]_{\mathrm{o}}}{[K^+]_{\mathrm{o}} + K_{\mathrm{m,Ko}}}\right).$$

I_{K1}

$$\overline{G}_{\mathrm{K1}} = 0.5625 \cdot \sqrt{\frac{[K^+]_{\mathrm{o}}}{5.4}}$$

$$E_{\mathrm{K1}} = \frac{RT}{F} \cdot \ln\left(\frac{[K^+]_{\mathrm{o}}}{[K^+]_{\mathrm{i}}}\right)$$

$$\alpha_{\mathrm{K1}} = \frac{1.02}{1 + \exp(0.2385 \cdot (V_{\mathrm{m}} - E_{\mathrm{K1}} - 59.215))}$$

$$\beta_{\mathrm{K1}} = \frac{0.49124 \cdot \exp(0.08032 \cdot (V_{\mathrm{m}} - E_{\mathrm{K1}} + 5.476)) + \exp(0.06175 \cdot (V_{\mathrm{m}} - E_{\mathrm{K1}} - 594.31))}{1 + \exp(-0.5143 \cdot (V_{\mathrm{m}} - E_{\mathrm{K1}} + 4.753))}$$

$$K_1 = \frac{\alpha_{\mathrm{K1}}}{\alpha_{\mathrm{K1}} + \beta_{\mathrm{K1}}}$$

$$I_{\mathrm{K1}} = \overline{G}_{\mathrm{K1}} \cdot K_1 \cdot (V_{\mathrm{m}} - E_{\mathrm{K1}}).$$

$I_{p,Ca}$

$$\overline{G}_{\mathrm{p,Ca}} = 1$$

$I_{\mathrm{p,Ca}}$

$$= \overline{G}_{\mathrm{p,Ca}} \cdot \frac{[Ca^{2+}]_{\mathrm{i}}}{(0.0005 + [Ca^{2+}]_{\mathrm{i}})} \cdot \frac{1}{1 + \exp\left(\dfrac{0.00012 - [Ca^{2+}]_{\mathrm{i}}}{0.00001}\right)}.$$

SR fluxes

$$I_{\mathrm{up}} = \overline{I_{\mathrm{up}}} \cdot \frac{[Ca^{2+}]_{\mathrm{i}}}{[Ca^{2+}]_{\mathrm{i}} + K_{\mathrm{m,up}}}$$

$$\overline{I_{\mathrm{up}}} = 0.017325 \,\mathrm{mM/ms}; K_{\mathrm{m,up}} = 0.00092 \,\mathrm{mM}$$

$$\overline{NSR} = 15 \,\mathrm{mM}$$

$$I_{\mathrm{leak}} = \frac{0.00875}{\overline{NSR}} \cdot [Ca^{2+}]_{\mathrm{NSR}}$$

$$\tau_{\mathrm{tr}} = 120 \,\mathrm{ms}$$

$$I_{\mathrm{tr}} = \frac{[Ca^{2+}]_{\mathrm{NSR}} - [Ca^{2+}]_{\mathrm{JSR}}}{\tau_{\mathrm{tr}}}.$$

Ca^{2+} buffers in myoplasm

$$\text{Buffered } [trpn] = [\overline{trpn}] \cdot \frac{[Ca^{2+}]_i}{[Ca^{2+}]_i + K_{m,trpn}}$$

$$\text{Buffered } [cmdn] = [\overline{cmdn}] \cdot \frac{[Ca^{2+}]_i}{[Ca^{2+}]_i + K_{m,cmdn}}$$

$$[\overline{trpn}] = 0.07 \text{ mM}; [\overline{cmdn}] = 0.05 \text{ mM};$$

$$K_{m,trpn} = 0.0005 \text{ mM}; K_{m,cmdn} = 0.00238 \text{ mM}.$$

Ca^{2+} buffer in JSR

$$\text{Buffered } [csqn] = [\overline{csqn}] \cdot \frac{[Ca^{2+}]_{JSR}}{[Ca^{2+}]_{JSR} + K_{m,csqn}}$$

$$[\overline{csqn}] = 10 \text{ mM}; K_{m,csqn} = 0.8 \text{ mM}.$$

Intracellular ion concentrations

a. Ca^{2+}

$$\beta_{myo} = \frac{1}{1 + \frac{[trpn] \cdot K_{m,trpn}}{(K_{m,trpn} + [Ca^{2+}]_i)^2} + \frac{[cmdn] \cdot K_{m,cmdn}}{(K_{m,cmdn} + [Ca^{2+}]_i)^2}}$$

$$\frac{d[Ca^{2+}]_i}{dt} = -\beta_{myo} \cdot \left((I_{Ca,t} - (I_{Ca(L)} - 2 \cdot I_{NaCa,ss})) \right.$$
$$\left. \cdot \frac{A_{cap}}{V_{myo} \cdot z_{ca} \cdot F} + (I_{up} - I_{leak}) \cdot \frac{V_{NSR}}{V_{myo}} - I_{diff,Ca} \cdot \frac{V_{ss}}{V_{myo}} \right)$$

b. Na$^+$

$$\frac{d[Na^+]_i}{dt} = -\left((I_{Na,t} - (I_{Ca,Na} + 3 \cdot I_{NaCa,ss})) \right.$$
$$\left. \cdot \frac{A_{cap}}{V_{myo} \cdot F} - I_{diff,Na} \cdot \frac{V_{ss}}{V_{myo}} \right)$$

c. K$^+$

$$\frac{d[K^+]_i}{dt} = -\left((I_{K,t} - I_{Ca,K}) \cdot \frac{A_{cap}}{V_{myo} \cdot F} - I_{diff,K} \cdot \frac{V_{ss}}{V_{myo}} \right).$$

SR calcium concentrations

a. JSR

$$\beta_{JSR} = \frac{1}{1 + \frac{[csqn] \cdot K_{m,csqn}}{(K_{m,csqn} + [Ca^{2+}]_{JSR})^2}}$$

$$\frac{d[Ca^{2+}]_{JSR}}{dt} = \beta_{JSR} \cdot (I_{tr} - I_{rel})$$

b. NSR

$$\frac{d[Ca^{2+}]_{NSR}}{dt} = I_{up} - I_{leak} - I_{tr} \cdot \frac{V_{JSR}}{V_{NSR}}.$$

Subspace concentrations

a. Ca^{2+}

$$\beta_{ss} = \frac{1}{1 + \frac{\overline{BSR} \cdot K_{m,BSR}}{(K_{m,BSR} + [Ca^{2+}]_{ss})^2} + \frac{\overline{BSL} \cdot K_{m,BSL}}{(K_{m,BSL} + [Ca^{2+}]_{ss})^2}}$$

$$\overline{BSR} = 0.047 \text{ mM}; K_{m,BSR} = 0.00087 \text{ mM}$$

$$\overline{BSL} = 2.124 \text{ mM}; K_{m,BSL} = 0.127 \text{ mM}$$

$$I_{diff,Ca} = \frac{[Ca^{2+}]_{ss} - [Ca^{2+}]_i}{\tau_{diff}}$$

$$\tau_{diff} = 0.1 \text{ ms}$$

$$\frac{d[Ca^{2+}]_{ss}}{dt} = -\beta_{ss} \cdot \left((I_{Ca(L)} - 2 \cdot I_{NaCa,ss}) \cdot \frac{A_{cap}}{V_{ss} \cdot z_{ca} \cdot F} \right.$$
$$\left. -I_{rel} \cdot \frac{V_{JSR}}{V_{ss}} + I_{diff,Ca} \right).$$

b. Na$^+$

$$I_{diff,Na} = \frac{[Na^+]_{ss} - [Na^+]_i}{\tau_{diff}}$$

$$\frac{d[Na^+]_{ss}}{dt} = -\left((I_{Ca,Na} + 3 \cdot I_{NaCa,ss}) \cdot \frac{A_{cap}}{V_{ss} \cdot F} + I_{diff,Na} \right)$$

c. K$^+$

$$I_{diff,K} = \frac{[K^+]_{ss} - [K^+]_i}{\tau_{diff}}$$

$$\frac{d[K^+]_{ss}}{dt} = -\left((I_{Ca,K}) \cdot \frac{A_{cap}}{V_{ss} \cdot F} + I_{diff,K} \right).$$

Conservative current stimulus

For the duration of the stimulation

$$I_{K,t} = I_{K,t} + I_{stim}$$

V_m

$$\frac{dV_m}{dt} = \frac{-I_{tot}}{C_m}.$$

Cell geometry

$$\text{Length}(L) = 0.01 \text{ cm}; \text{radius}(r) = 0.0011 \text{ cm}$$

$$\text{Cell volume}: V_{cell} = \pi \cdot r^2 \cdot L = 38 \times 10^{-6} \, \mu L$$

$$\text{Geometric membrane area}: A_{geo} = 2\pi \cdot r^2 + 2\pi \cdot r \cdot L$$
$$= 0.767 \times 10^{-4} \text{ cm}^2$$

$$\text{Capacitive membrane area}: A_{cap} = R_{CG} \cdot A_{geo}$$
$$= 1.534 \times 10^{-4} \text{ cm}^2$$

Myoplasm volume: $V_{\mathrm{myo}} = V_{\mathrm{cell}} \cdot 68\% = 25.84 \times 10^{-6}\,\mu\mathrm{L}$

Mitochondria volume: $V_{\mathrm{mito}} = V_{\mathrm{cell}} \cdot 24\% = 9.88 \times 10^{-6}\,\mu\mathrm{L}$

SR volume: $V_{\mathrm{SR}} = V_{\mathrm{cell}} \cdot 6\% = 2.28 \times 10^{-6}\,\mu\mathrm{L}$

NSR volume: $V_{\mathrm{NSR}} = V_{\mathrm{cell}} \cdot 5.52\% = 2.098 \times 10^{-6}\,\mu\mathrm{L}$

JSR volume: $V_{\mathrm{JSR}} = V_{\mathrm{cell}} \cdot 0.48\% = 0.182 \times 10^{-6}\,\mu\mathrm{L}$

Subspace volume: $V_{\mathrm{ss}} = V_{\mathrm{cell}} \cdot 2\% = 0.76 \times 10^{-6}\,\mu\mathrm{L}$.

Derivation of subspace volume

We assume a myocyte with a radius of 11 μm and length of 100 μm with Z-lines spaced by 1.85 μm. T-tubules protrude into the myocyte along the Z-lines with spacing of 1.5 μm. With these values, we compute 54 Z-lines per myocyte with 46 t-tubules per Z-line for a total of 2484 t-tubules per myocyte. The diameter of each t-tubule is 0.3 μm and the distance between the SR membrane and the t-tubule is 0.02 μm (15). The volume of subspace along the length of a single t-tubule to the center of the myocyte is:

$$11\,\mu\mathrm{m} \cdot \pi \cdot \left(\frac{0.340\mu\mathrm{m}}{2}\right)^2 - 11\,\mu\mathrm{m} \cdot \pi \cdot \left(\frac{0.300\,\mu\mathrm{m}}{2}\right)^2$$
$$= 0.2212\,\mu\mathrm{m}^3$$

The total subspace volume $= 2484 \cdot 0.2212\,\mu\mathrm{m}^3 = 550\,\mu\mathrm{m}^3$
$$= 5.5 \times 10^{-7}\,\mu\mathrm{L},$$

which is $100 \cdot (5.5 \times 10^{-7}\,\mu\mathrm{L})/(38 \times 10^{-6}\,\mu\mathrm{L}) = 1.5\%$ of the whole cell volume. In the model, we round to 2%.

Initial ionic concentrations and markov model state residencies

End diastolic steady-state values for the model paced at $CL = 1000$ ms.

$$[\mathrm{Ca}^{2+}]_{\mathrm{i}} = 8.21 \times 10^{-5}\,\mathrm{mM}$$
$$[\mathrm{Ca}^{2+}]_{\mathrm{ss}} = 6.72 \times 10^{-5}\,\mathrm{mM}$$
$$[\mathrm{K}^+]_{\mathrm{i}} = 137.6\,\mathrm{mM}$$
$$[\mathrm{K}^+]_{\mathrm{ss}} = 137.6\,\mathrm{mM}$$
$$[\mathrm{Na}^+]_{\mathrm{i}} = 10.71\,\mathrm{mM}$$
$$[\mathrm{Na}^+]_{\mathrm{ss}} = 10.71\,\mathrm{mM}$$
$$[\mathrm{Ca}^{2+}]_{\mathrm{NSR}} = 2.553\,\mathrm{mM}$$
$$[\mathrm{Ca}^{2+}]_{\mathrm{JSR}} = 2.479\,\mathrm{mM}$$
$$[\mathrm{Ca}^{2+}]_{\mathrm{o}} = 1.8\,\mathrm{mM}$$
$$[\mathrm{K}^+]_{\mathrm{o}} = 4.5\,\mathrm{mM}$$
$$[\mathrm{Na}^+]_{\mathrm{o}} = 130\,\mathrm{mM}.$$

L-type Ca^{2+} channel

$$C_0 = 0.923$$
$$C_1 = 0.049$$

$$C_2 = 0$$
$$C_3 = 0$$
$$C_{0\mathrm{Ca}} = 0.025$$
$$C_{1\mathrm{Ca}} = 0.003$$
$$C_{2\mathrm{Ca}} = 0$$
$$C_{3\mathrm{Ca}} = 0$$
$$O = 0$$
$$I_{\mathrm{Ca}} = 0$$
$$I_{\mathrm{Vf}} = 0$$
$$I_{\mathrm{VfCa}} = 0$$
$$I_{\mathrm{Vs}} = 0$$
$$I_{\mathrm{VsCa}} = 0$$

RyR

$$C_1 = 0.890$$
$$C_2 = 0.021$$
$$C_3 = 0.003$$
$$C_4 = 0.001$$
$$O = 0$$
$$I_1 = 0.082$$
$$I_2 = 0.002$$
$$I_3 = 0.001$$
$$I_4 = 0$$
$$I_5 = 0$$

Kinetics for G406R CA$_\mathrm{V}$1.2

$$\alpha = 0.925 \cdot \exp(V_{\mathrm{m}}/30)$$
$$\beta = 0.39 \cdot \exp(-V_{\mathrm{m}}/40)$$
$$\alpha_0 = 4 \cdot \alpha$$
$$\alpha_1 = 3 \cdot \alpha$$
$$\alpha_2 = 2 \cdot \alpha$$
$$\alpha_3 = \alpha$$
$$\beta_0 = \beta$$
$$\beta_1 = 2 \cdot \beta$$
$$\beta_2 = 3 \cdot \beta$$
$$\beta_3 = 4 \cdot \beta$$
$$\gamma_{\mathrm{f}} = 0.0245 \cdot \exp(V_{\mathrm{m}}/10)$$
$$\gamma_{\mathrm{s}} = 0.0005 \cdot \exp(-V_{\mathrm{m}}/40)$$
$$\phi_{\mathrm{f}} = 0.02 \cdot \exp(V_{\mathrm{m}}/500)$$
$$\phi_{\mathrm{s}} = 0.0037 \cdot \exp(-V_{\mathrm{m}}/60)$$
$$\lambda_{\mathrm{f}} = 0.35 \cdot \exp(-V_{\mathrm{m}}/300)$$
$$\lambda_{\mathrm{s}} = 0.004 \cdot \exp(V_{\mathrm{m}}/80)$$
$$\omega_{\mathrm{f}} = (\beta_3 \cdot \lambda_{\mathrm{f}} \cdot \gamma_{\mathrm{f}})/(\alpha_3 \cdot \phi_{\mathrm{f}})$$

$$\omega_s = (\beta_3 \cdot \lambda_s \cdot \gamma_s)/(\alpha_3 \cdot \phi_s)$$

$$\omega_{sf} = (\lambda_s \cdot \phi_f)/\lambda_f$$

$$\omega_{fs} = \phi_s$$

$$\delta = \frac{4}{1 + 1/[Ca^{2+}]_{ss}}$$

$$\theta = 0.01.$$

REFERENCES

1. Hodgkin, A. L., and A. F. Huxley. 1952. A quantitative description of membrane current and its application to conduction and excitation in nerve. *J. Physiol.* 117:500–544.

2. Rudy, Y., and J. Silva. 2006. Computational biology in the study of cardiac ion channels and cell electrophysiology. *Q. Rev. Biophys.* 39:57–116.

3. Clancy, C. E., and Y. Rudy. 1999. Linking a genetic defect to its cellular phenotype in a cardiac arrhythmia. *Nature.* 400:566–569.

4. Clancy, C. E., and Y. Rudy. 2002. Na(+) channel mutation that causes both Brugada and long-QT syndrome phenotypes: a simulation study of mechanism. *Circulation.* 105:1208–1213.

5. Clancy, C. E., and Y. Rudy. 2001. Cellular consequences of HERG mutations in the long QT syndrome: precursors to sudden cardiac death. *Cardiovasc. Res.* 50:301–313.

6. Silva, J., and Y. Rudy. 2005. Subunit interaction determines IKs participation in cardiac repolarization and repolarization reserve. *Circulation.* 112:1384–1391.

7. Clancy, C. E., Z. I. Zhu, and Y. Rudy. 2006. Pharmacogenetics and anti-arrhythmic drug therapy: a theoretical investigation. *Am. J. Physiol.* In press.

8. Sun, H., N. Leblanc, and S. Nattel. 1997. Mechanisms of inactivation of L-type calcium channels in human atrial myocytes. *Am. J. Physiol.* 272:H1625–H1635.

9. Hund, T. J., and Y. Rudy. 2004. Rate dependence and regulation of action potential and calcium transient in a canine cardiac ventricular cell model. *Circulation.* 110:3168–3174.

10. Shaw, R. M., and Y. Rudy. 1997. Ionic mechanisms of propagation in cardiac tissue. Roles of the sodium and L-type calcium currents during reduced excitability and decreased gap junction coupling. *Circ. Res.* 81:727–741.

11. Kléber, A. G., and Y. Rudy. 2004. Basic mechanisms of cardiac impulse propagation and associated arrhythmias. *Physiol. Rev.* 84:431–488.

12. Bers, D. M. 2001. Excitation-Contraction Coupling and Cardiac Contractile Force. Kluwer Academic Publishers, Dordrecht, The Netherlands.

13. Splawski, I., K. W. Timothy, L. M. Sharpe, N. Decher, P. Kumar, R. Bloise, C. Napolitano, P. J. Schwartz, R. M. Joseph, K. Condouris, H. Tager-Flusberg, S. G. Priori, et al. 2004. Ca(V)1.2 calcium channel dysfunction causes a multisystem disorder including arrhythmia and autism. *Cell* 119:19–31.

14. Splawski, I., K. W. Timothy, N. Decher, P. Kumar, F. B. Sachse, A. H. Beggs, M. C. Sanguinetti, and M. T. Keating. 2005. Severe arrhythmia disorder caused by cardiac L-type calcium channel mutations. *Proc. Natl. Acad. Sci. USA.* 102:8089–8096.

15. Guatimosim, S., K. Dilly, L. F. Santana, M. Saleet Jafri, E. A. Sobie, and W. J. Lederer. 2002. Local Ca(2+) signaling and EC coupling in heart: Ca(2+) sparks and the regulation of the [Ca(2+)]i transient. *J. Mol. Cell. Cardiol.* 34:941–950.

16. Fill, M., and J. A. Copello. 2002. Ryanodine receptor calcium release channels. *Physiol. Rev.* 82:893–922.

17. Stern, M. D., L. S. Song, H. Cheng, J. S. Sham, H. T. Yang, K. R. Boheler, and E. Ríos. 1999. Local control models of cardiac excitation-contraction coupling. A possible role for allosteric interactions between ryanodine receptors. *J. Gen. Physiol.* 113:469–489.

18. Hinch, R., J. L. Greenstein, A. J. Tanskanen, L. Xu, and R. L. Winslow. 2004. A simplified local control model of calcium-induced calcium release in cardiac ventricular myocytes. *Biophys. J.* 87:3723–3736.

19. Hadley, R. W., and W. J. Lederer. 1991. Ca2+ and voltage inactivate Ca2+ channels in guinea-pig ventricular myocytes through independent mechanisms. *J. Physiol.* 444:257–268.

20. Stotz, S. C., and G. W. Zamponi. 2001. Structural determinants of fast inactivation of high voltage-activated Ca(2+) channels. *Trends Neurosci.* 24:176–181.

21. Dafi, O., L. Berrou, Y. Dodier, A. Raybaud, R. Sauvé, and L. Parent. 2004. Negatively charged residues in the N-terminal of the AID helix confer slow voltage dependent inactivation gating to CaV1.2. *Biophys. J.* 87:3181–3192.

22. Peterson, B. Z., C. D. DeMaria, J. P. Adelman, and D. T. Yue. 1999. Calmodulin is the Ca2+ sensor for Ca2+ -dependent inactivation of L-type calcium channels. *Neuron.* 22:549–558.

23. Zühlke, R. D., G. S. Pitt, K. Deisseroth, R. W. Tsien, and H. Reuter. 1999. Calmodulin supports both inactivation and facilitation of L-type calcium channels. *Nature.* 399:159–162.

24. Zühlke, R. D., G. S. Pitt, R. W. Tsien, and H. Reuter. 2000. Ca2+-sensitive inactivation and facilitation of L-type Ca2+ channels both depend on specific amino acid residues in a consensus calmodulin-binding motif in the(alpha)1C subunit. *J. Biol. Chem.* 275:21121–21129.

25. Alseikhan, B. A., C. D. DeMaria, H. M. Colecraft, and D. T. Yue. 2002. Engineered calmodulins reveal the unexpected eminence of Ca2+ channel inactivation in controlling heart excitation. *Proc. Natl. Acad. Sci. USA.* 99:17185–17190.

26. Liang, H., C. D. DeMaria, M. G. Erickson, M. X. Mori, B. A. Alseikhan, and D. T. Yue. 2003. Unified mechanisms of Ca2+ regulation across the Ca2+ channel family. *Neuron.* 39:951–960.

27. Jafri, M. S., J. J. Rice, and R. L. Winslow. 1998. Cardiac Ca2+ dynamics: the roles of ryanodine receptor adaptation and sarcoplasmic reticulum load. *Biophys. J.* 74:1149–1168.

28. Yue, D. T., P. H. Backx, and J. P. Imredy. 1990. Calcium-sensitive inactivation in the gating of single calcium channels. *Science.* 250:1735–1738.

29. Ferreira, G., E. Ríos, and N. Reyes. 2003. Two components of voltage-dependent inactivation in Ca(v)1.2 channels revealed by its gating currents. *Biophys. J.* 84:3662–3678.

30. Luo, C. H., and Y. Rudy. 1994. A dynamic model of the cardiac ventricular action potential. I. Simulations of ionic currents and concentration changes. *Circ. Res.* 74:1071–1096.

31. Zeng, J., K. R. Laurita, D. S. Rosenbaum, and Y. Rudy. 1995. Two components of the delayed rectifier K+ current in ventricular myocytes of the guinea pig type. Theoretical formulation and their role in repolarization. *Circ. Res.* 77:140–152.

32. Faber, G. M., and Y. Rudy. 2000. Action potential and contractility changes in [Na(+)]i overloaded cardiac myocytes: a simulation study. *Biophys. J.* 78:2392–2404.

33. Gao, T., T. S. Puri, B. L. Gerhardstein, A. J. Chien, R. D. Green, and M. M. Hosey. 1997. Identification and subcellular localization of the subunits of L-type calcium channels and adenylyl cyclase in cardiac myocytes. *J. Biol. Chem.* 272:19401–19407.

34. Gathercole, D. V., D. J. Colling, J. N. Skepper, Y. Takagishi, A. J. Levi, and N. J. Severs. 2000. Immunogold-labeled L-type calcium channels are clustered in the surface plasma membrane overlying junctional sarcoplasmic reticulum in guinea-pig myocytes-implications for excitation-contraction coupling in cardiac muscle. *J. Mol. Cell. Cardiol.* 32:1981–1994.

35. Frank, J. S., G. Mottino, D. Reid, R. S. Molday, and K. D. Philipson. 1992. Distribution of the Na(+)-Ca2+ exchange protein in mammalian cardiac myocytes: an immunofluorescence and immunocolloidal gold-labeling study. *J. Cell Biol.* 117:337–345.

36. Kieval, R. S., R. J. Bloch, G. E. Lindenmayer, A. Ambesi, and W. J. Lederer. 1992. Immunofluorescence localization of the Na-Ca exchanger in heart cells. *Am. J. Physiol.* 263:C545–C550.

37. Han, C., P. Tavi, and M. Weckström. 2002. Role of the Na(+)-Ca(2+) exchanger as an alternative trigger of CICR in mammalian cardiac myocytes. *Biophys. J.* 82:1483–1496.

38. Smith, G. D., J. E. Keizer, M. D. Stern, W. J. Lederer, and H. Cheng. 1998. A simple numerical model of calcium spark formation and detection in cardiac myocytes. *Biophys. J.* 75:15–32.

39. Fill, M., A. Zahradníková, C. A. Villalba-Galea, I. Zahradník, A. L. Escobar, and S. Györke. 2000. Ryanodine receptor adaptation. *J. Gen. Physiol.* 116:873–882.

40. Zahradníková, A., and I. Zahradník. 1995. Description of modal gating of the cardiac calcium release channel in planar lipid membranes. *Biophys. J.* 69:1780–1788.

41. Zahradník, I., S. Györke, and A. Zahradníková. 2005. Calcium activation of ryanodine receptor channels—reconciling RyR gating models with tetrameric channel structure. *J. Gen. Physiol.* 126:515–527.

42. Ikemoto, N., M. Ronjat, L. G. Mészáros, and M. Koshita. 1989. Postulated role of calsequestrin in the regulation of calcium release from sarcoplasmic reticulum. *Biochemistry.* 28:6764–6771.

43. Ikemoto, N., B. Antoniu, J. J. Kang, L. G. Mészáros, and M. Ronjat. 1991. Intravesicular calcium transient during calcium release from sarcoplasmic reticulum. *Biochemistry.* 30:5230–5237.

44. Kawasaki, T., and M. Kasai. 1994. Regulation of calcium channel in sarcoplasmic reticulum by calsequestrin. *Biochem. Biophys. Res. Commun.* 199:1120–1127.

45. Hidalgo, C., P. Donoso, and P. H. Rodriguez. 1996. Protons induce calsequestrin conformational changes. *Biophys. J.* 71:2130–2137.

46. Györke, I., N. Hester, L. R. Jones, and S. Györke. 2004. The role of calsequestrin, triadin, and junctin in conferring cardiac ryanodine receptor responsiveness to luminal calcium. *Biophys. J.* 86:2121–2128.

47. Guo, W., and K. P. Campbell. 1995. Association of triadin with the ryanodine receptor and calsequestrin in the lumen of the sarcoplasmic reticulum. *J. Biol. Chem.* 270:9027–9030.

48. Zhang, L., J. Kelley, G. Schmeisser, Y. M. Kobayashi, and L. R. Jones. 1997. Complex formation between junctin, triadin, calsequestrin, and the ryanodine receptor. Proteins of the cardiac junctional sarcoplasmic reticulum membrane. *J. Biol. Chem.* 272:23389–23397.

49. Hund, T. J., J. P. Kucera, N. F. Otani, and Y. Rudy. 2001. Ionic charge conservation and long-term steady state in the Luo-Rudy dynamic cell model. *Biophys. J.* 81:3324–3331.

50. Rose, W. C., C. W. Balke, W. G. Wier, and E. Marban. 1992. Macroscopic and unitary properties of physiological ion flux through L-type Ca2+ channels in guinea-pig heart cells. *J. Physiol.* 456:267–284.

51. Findlay, I. 2002. Voltage-dependent inactivation of L-type Ca2+ currents in guinea-pig ventricular myocytes. *J. Physiol.* 545:389–397.

52. Cavalié, A., D. Pelzer, and W. Trautwein. 1986. Fast and slow gating behaviour of single calcium channels in cardiac cells. Relation to activation and inactivation of calcium-channel current. *Pflugers Arch.* 406:241–258.

53. Höfer, G. F., K. Hohenthanner, W. Baumgartner, K. Groschner, N. Klugbauer, F. Hofmann, and C. Romanin. 1997. Intracellular Ca2+ inactivates L-type Ca2+ channels with a Hill coefficient of approximately 1 and an inhibition constant of approximately 4 microM by reducing channel's open probability. *Biophys. J.* 73:1857–1865.

54. Vornanen, M., and N. Shepherd. 1997. Restitution of contractility in single ventricular myocytes of guinea pig heart. *Cardiovasc. Res.* 33:611–622.

55. Findlay, I. 2004. Physiological modulation of inactivation in L-type Ca2+ channels: one switch. *J. Physiol.* 554:275–283.

56. Shannon, T. R., K. S. Ginsburg, and D. M. Bers. 2000. Potentiation of fractional sarcoplasmic reticulum calcium release by total and free intra-sarcoplasmic reticulum calcium concentration. *Biophys. J.* 78:334–343.

57. Beuckelmann, D. J., and W. G. Wier. 1988. Mechanism of release of calcium from sarcoplasmic reticulum of guinea-pig cardiac cells. *J. Physiol.* 405:233–255.

58. Song, L. S., Y. Pi, S. J. Kim, A. Yatani, S. Guatimosim, R. K. Kudej, Q. Zhang, H. Cheng, L. Hittinger, B. Ghaleh, D. E. Vatner, W. J. Lederer, and S. F. Vatner. 2005. Paradoxical cellular Ca2+ signaling in severe but compensated canine left ventricular hypertrophy. *Circ. Res.* 97:457–464.

59. Grantham, C. J., and M. B. Cannell. 1996. Ca2+ influx during the cardiac action potential in guinea pig ventricular myocytes. *Circ. Res.* 79:194–200.

60. Choi, B. R., and G. Salama. 2000. Simultaneous maps of optical action potentials and calcium transients in guinea-pig hearts: mechanisms underlying concordant alternans. *J. Physiol.* 529:171–188.

61. Bosch, R. F., R. Gaspo, A. E. Busch, H. J. Lang, G. R. Li, and S. Nattel. 1998. Effects of the chromanol 293B, a selective blocker of the slow, component of the delayed rectifier K+ current, on repolarization in human and guinea pig ventricular myocytes. *Cardiovasc. Res.* 38:441–450.

62. Wang, D. Y., S. W. Chae, Q. Y. Gong, and C. O. Lee. 1988. Role of aiNa in positive force-frequency staircase in guinea pig papillary muscle. *Am. J. Physiol.* 255:C798–C807.

63. Szentesi, P., C. Pignier, M. Egger, E. G. Kranias, and E. Niggli. 2004. Sarcoplasmic reticulum Ca2+ refilling controls recovery from Ca2+-induced Ca2+ release refractoriness in heart muscle. *Circ. Res.* 95:807–813.

64. Ferreira, G., J. Yi, E. Ríos, and R. Shirokov. 1997. Ion-dependent inactivation of barium current through L-type calcium channels. *J. Gen. Physiol.* 109:449–461.

65. Hadley, R. W., and J. R. Hume. 1987. An intrinsic potential-dependent inactivation mechanism associated with calcium channels in guinea-pig myocytes. *J. Physiol.* 389:205–222.

66. Linz, K. W., and R. Meyer. 1998. Control of L-type calcium current during the action potential of guinea-pig ventricular myocytes. *J. Physiol.* 513:425–442.

67. Findlay, I. 2002. Voltage- and cation-dependent inactivation of L-type Ca2+ channel currents in guinea-pig ventricular myocytes. *J Physiol* 541(Pt) 3:731–740.

68. Findlay, I. 2002. Beta-adrenergic and muscarinic agonists modulate inactivation of L-type Ca2+ channel currents in guinea-pig ventricular myocytes. *J. Physiol.* 545:375–388.

69. Findlay, I. 2002. beta-Adrenergic stimulation modulates Ca2+- and voltage-dependent inactivation of L-type Ca2+ channel currents in guinea-pig ventricular myocytes. *J. Physiol.* 541:741–751.

70. Pitt, G. S., R. D. Zühlke, A. Hudmon, H. Schulman, H. Reuter, and R. W. Tsien. 2001. Molecular basis of calmodulin tethering and Ca2+-dependent inactivation of L-type Ca2+ channels. *J. Biol. Chem.* 276:30794–30802.

71. Isaev, D., K. Solt, O. Gurtovaya, J. P. Reeves, and R. Shirokov. 2004. Modulation of the voltage sensor of L-type Ca2+ channels by intracellular Ca2+. *J. Gen. Physiol.* 123:555–571.

72. Hess, P., J. B. Lansman, and R. W. Tsien. 1986. Calcium channel selectivity for divalent and monovalent cations. Voltage and concen-

tration dependence of single channel current in ventricular heart cells. *J. Gen. Physiol.* 88:293–319.

73. Lansman, J. B., P. Hess, and R. W. Tsien. 1986. Blockade of current through single calcium channels by Cd2+, Mg2+, and Ca2+. Voltage and concentration dependence of calcium entry into the pore. *J. Gen. Physiol.* 88:321–347.

74. Lee, A., H. Zhou, T. Scheuer, and W. A. Catterall. 2003. Molecular determinants of Ca(2+)/calmodulin-dependent regulation of Ca(v)2.1 channels. *Proc. Natl. Acad. Sci. USA.* 100:16059–16064.

75. Dzhura, I., Y. Wu, R. J. Colbran, J. R. Balser, and M. E. Anderson. 2000. Calmodulin kinase determines calcium-dependent facilitation of L-type calcium channels. *Nat. Cell Biol.* 2:173–177.

76. Hudmon, A., H. Schulman, J. Kim, J. M. Maltez, R. W. Tsien, and G. S. Pitt. 2005. CaMKII tethers to L-type Ca2+ channels, establishing a local and dedicated integrator of Ca2+ signals for facilitation. *J. Cell Biol.* 171:537–547.

77. Kamp, T. J., and J. W. Hell. 2000. Regulation of cardiac L-type calcium channels by protein kinase A and protein kinase C. *Circ. Res.* 87:1095–1102.

78. Saucerman, J. J., L. L. Brunton, A. P. Michailova, and A. D. McCulloch. 2003. Modeling beta-adrenergic control of cardiac myocyte contractility in silico. *J. Biol. Chem.* 278:47997–48003.

79. Sobie, E. A., K. W. Dilly, J. dos Santos Cruz, W. J. Lederer, and M. S. Jafri. 2002. Termination of cardiac Ca(2+) sparks: an investigative mathematical model of calcium-induced calcium release. *Biophys. J.* 83:59–78.

80. Greenstein, J. L., and R. L. Winslow. 2002. An integrative model of the cardiac ventricular myocyte incorporating local control of Ca2+ release. *Biophys. J.* 83:2918–2945.

81. Greenstein, J. L., R. Hinch, and R. L. Winslow. 2006. Mechanisms of excitation-contraction coupling in an integrative model of the cardiac ventricular myocyte. *Biophys. J.* 90:77–91.

82. Chu, A., M. Fill, E. Stefani, and M. L. Entman. 1993. Cytoplasmic Ca2+ does not inhibit the cardiac muscle sarcoplasmic reticulum ryanodine receptor Ca2+ channel, although Ca(2+)-induced Ca2+ inactivation of Ca2+ release is observed in native vesicles. *J. Membr. Biol.* 135:49–59.

83. Stern, M. D. 1992. Theory of excitation-contraction coupling in cardiac muscle. *Biophys. J.* 63:497–517.

84. Rice, J. J., M. S. Jafri, and R. L. Winslow. 1999. Modeling gain and gradedness of Ca2+ release in the functional unit of the cardiac diadic space. *Biophys. J.* 77:1871–1884.

85. Dura, M., I. Zahradník, and A. Zahradníková. 2003. Kinetics of cardiac RyR channel gating studied at high temporal resolution. *Physiol. Res.* 52:571–578.

86. Brochet, D. X., D. Yang, A. Di Maio, W. J. Lederer, C. Franzini-Armstrong, and H. Cheng. 2005. Ca2+ blinks: rapid nanoscopic store calcium signaling. *Proc. Natl. Acad. Sci. USA.* 102:3099–3104.